

---

# Sign-Aware Gated Sparse Autoencoders: Modeling Anticorrelated Features with Bi-Jump-ReLU Activations

---

Bartosz Wiecech   Zmnako Awrahman   Marcin Czelej  
Victor Hugo Jaramillo Velasquez   Wioletta Stobieniecka  
Amazon Web Services  
bartwie@amazon.com

## Abstract

Sparse Autoencoders (SAEs) have emerged as a common tool for extracting interpretable features from Large Language Models. However, standard SAEs enforce non-negativity on latent activations, forcing the model to learn separate features for diametrically opposed concepts (e.g., “pressure too high” vs. “pressure too low”). This wastes dictionary capacity when features are naturally anticorrelated. We propose the *Sign-Aware Gated SAE* (SA-GSAE), whose mechanism is *two-sided gated sparsity with signed magnitude and auxiliary supervision*: a polarity-sensitive gate selects support on either sign, a signed-magnitude path avoids  $L_1$  shrinkage, and an auxiliary reconstruction prevents gate collapse. *Bipolar sharing* – one latent encoding both signs along a shared direction – is a consequence of this architecture, realised via a new *Bi-Jump-ReLU* activation; width/parameter accounting shows sign-awareness stays parameter-efficient even when anticorrelated pairs are rare. On real LLM activations across three mid-depth hookpoints on Pythia-1B and SmoLLM3-3B (6 cells, 3 seeds), a half-width SA-GSAE at width  $H$  strictly Pareto-dominates a full-width Gated SAE at  $2H$  over the entire swept  $L_0$  overlap on 3 of 6 cells (both MLP-output hookpoints and `resid-mid/Pythia-1B`); on the remaining 3 cells it matches  $R^2$  to within 0.025 (max negative gap  $-0.008$ ) while cutting dead fraction by 0.35–0.62 absolute. SA-half’s dead-fraction reduction over Gated-full has sweep-geomean factors of  $\sim 100\times$  to  $500\times$  on MLP-output cells and Pythia-1B `resid`, and  $\sim 2\times$  to  $4\times$  on attention cells and SmoLLM3-3B `resid`. Ablations identify the two-sided gate and auxiliary loss as load-bearing (no auxiliary collapses LR to 0.27, 98% dead); tying  $r_i^+ = r_i^-$  is practically indistinguishable ( $|\Delta R^2| = 0.0015$ ) and we recommend this symmetric-magnitude variant as the default. The MLP-output capacity wins come from most latents carrying signal on both polarities; on attention, bipolar structure is instead concentrated in a small set of top-activation latents. At full width SA-GSAE is over-parameterized and exhibits a reproducible reconstruction collapse at the SmoLLM3-3B residual-stream site that the half-width variant entirely avoids, providing a second, site-specific motivation for the halved-width operating point.

## 1 Introduction

Mechanistic interpretability seeks human-usable descriptions of the internal computations of trained neural networks. In large language models, the most useful units of analysis often look less like individual neurons and more like feature directions or subspaces that participate in larger circuits [1–3]. A common working picture is that a token activation  $x$  is a superposition of a small number of latent features, even if this picture is only approximate in practice [4–7].

Classical sparse coding provides a natural formalism for this goal: given data vectors  $x \in \mathbb{R}^{d_{\text{in}}}$ , learn a dictionary  $D \in \mathbb{R}^{d_{\text{in}} \times H}$  and sparse coefficients  $z$  via

$$\min_{D, \{z^{(n)}\}} \sum_n \frac{1}{2} \|x^{(n)} - Dz^{(n)}\|_2^2 + \lambda \|z^{(n)}\|_1, \quad \|d_i\|_2 = 1, \quad (1)$$

where  $d_i$  denotes the  $i$ th column of  $D$  [8–11]. In this formulation the coefficients are signed: positive and negative values correspond to opposite directions along the same atom, unlike explicitly non-negative factorizations that enforce parts-based structure [12]. Sparse autoencoders amortize the per-example inference problem into a single forward pass, making sparse dictionary learning practical for large activation caches and highly overcomplete regimes [13].

Applied to LLM activations, SAEs are now a standard way to learn overcomplete dictionaries of residual-stream, MLP, or attention-output features [14–18]. Empirically, many learned latents align with human-interpretable concepts and support causal interventions, suggesting that SAEs can partially “resolve” superposition in practice [14–16]. At the same time, SAEs do not necessarily recover a unique or canonical basis of features, and theoretical analyses have begun to characterize their intrinsic amortization gaps and representational limits [19, 20]. Larger SAEs can reveal novel features, and meta-SAEs can decompose some latents into combinations of others [21]. Independently initialized SAEs trained on the same data can also recover substantially different feature sets [22]. We treat SAE dictionaries as useful decompositions rather than unique ground-truth bases.

A structural limitation of many popular SAE variants is non-negativity. ReLU-based and many gated models can only express  $f_i(x) \geq 0$ , so a bidirectional semantic axis is often represented by two latents, one for positive evidence and one for negative evidence. For axes such as “pressure too high” versus “pressure too low”, this sign splitting duplicates decoder capacity without adding geometric expressivity. Classical sparse coding does not require this, because coefficients are signed, and recent SAE work has started to make the same point explicitly, for example via AbsTopK [23].

Building on Gated SAEs, which separate support selection from magnitude estimation and thereby avoid classical  $L_1$  shrinkage [24], we introduce the *Sign-Aware Gated SAE*. A single latent can now represent positive or negative evidence along one decoder direction via a new *Bi-Jump-ReLU* activation. §3.3 gives a simple accounting argument showing that if a fraction  $p$  of features occurs as anticorrelated pairs, the required width drops to  $H_{\pm} = H(1 - p/2)$  and the construction becomes parameter-efficient once  $p \gtrsim 8/(d_{\text{in}} + 4)$ . We treat this as a structural sanity check, not an identifiability theorem.

## 2 Contributions

- Two-sided gated sparsity with signed magnitude and auxiliary supervision.** We introduce a polarity-sensitive Bi-Jump-ReLU activation combining a two-sided learnable dead zone with a signed-magnitude path, and train it with Gated-style auxiliary reconstruction. Ablations identify the two-sided gate and the auxiliary loss as the load-bearing components on real LLM activations (removing the auxiliary collapses LR to 0.27 and pushes dead fraction to 98%); bipolar sharing along a single decoder direction is a consequence of this architecture rather than an independent mechanism.
- A parameter-efficiency argument and a symmetric-magnitude default.** We give a simple width/parameter accounting argument for when sign awareness helps, and we test its most direct implication via a half-width versus full-width comparison on real LLM activations. Tying  $r_i^+ = r_i^-$  (symmetric-magnitude variant) is practically indistinguishable from independent per-polarity scaling on real activations ( $|\Delta R^2| = 0.0015$ ,  $|\Delta \text{MSE}| = 0.0002$  on Pythia-1B mlp\_out;  $\gamma_+/\gamma_-$  medians agree within  $\leq 0.05$  on every cell), and we therefore recommend it as the default.
- Controlled and real-model evidence.** On a controlled signed-axis benchmark, SA-GSAE matches a  $2\times$  width non-negative Gated SAE with half as many latents. On real activations, across three mid-depth hookpoints and two backbones, a half-width SA-GSAE cuts dead fraction by sweep-geomean factors of  $\sim 100\times$  to  $500\times$  on MLP-output cells and Pythia-1B resid and  $\sim 2\times$  to  $4\times$  on attention cells and SmolLM3-3B resid relative to a full-width Gated SAE, while matching or exceeding its reconstruction fidelity and strictly Pareto-dominating over the full swept  $L_0$  overlap on both MLP-output hookpoints and on

resid-mid/Pythia-1B (3 of 6 cells); on the remaining 3 cells  $\Delta R^2 \in [-0.008, -0.001]$  while cutting dead fraction by 0.35–0.62 absolute. The MLP-output capacity wins come from most latents carrying signal on both polarities; on attention, bipolar structure is instead concentrated in a small set of top-activation latents. At full width, SA-GSAE is over-parameterized and exhibits a reproducible collapse on the SmoLLM3-3B residual stream that the half-width variant avoids, further motivating the halved-width operating point.

To our knowledge, this is the first two-sided, gated, no-shrinkage SAE for signed feature sharing.

### 3 Method

We generalize the Gated SAE to signed activations while preserving its no-shrinkage separation between detection and magnitude [24]. Let  $D \in \mathbb{R}^{d_{\text{in}} \times H}$  denote the decoder dictionary, where  $H$  is the SAE width (the number of latents), with columns  $D_{:,i}$ , and let  $b_{\text{dec}} \in \mathbb{R}^{d_{\text{in}}}$  denote the decoder bias. As in standard SAE implementations, we center inputs by  $b_{\text{dec}}$  when forming encoder projections.

#### 3.1 The Bi-Jump-ReLU Activation

For each latent we use a decoder-aligned projection

$$t_i(x) = D_{:,i}^\top (x - b_{\text{dec}}), \quad i = 1, \dots, H. \quad (2)$$

The gate pre-activation is an affine transformation of this projection,

$$\pi_i(x) = \alpha_i t_i(x) + \beta_i, \quad (3)$$

with trainable per-latent parameters  $\alpha_i, \beta_i \in \mathbb{R}$ .

We introduce two threshold parameters  $\delta_i^+, \delta_i^- \geq 0$ , defining a learnable dead zone, and two unconstrained log-scale parameters  $r_i^+, r_i^- \in \mathbb{R}$ , which parameterize non-negative magnitude scales  $g_i^+ = \exp(r_i^+)$  and  $g_i^- = \exp(r_i^-)$ . Define the polarity variable

$$s_i(x) = \begin{cases} +1 & \text{if } \pi_i(x) > \delta_i^+ \\ -1 & \text{if } \pi_i(x) < -\delta_i^- \\ 0 & \text{otherwise.} \end{cases} \quad (4)$$

The signed latent activation is then

$$a_i(x) = \begin{cases} \text{ReLU}(g_i^+ t_i(x) + b_{\text{mag},i}) & \text{if } s_i(x) = +1 \\ -\text{ReLU}(-g_i^- t_i(x) + b_{\text{mag},i}) & \text{if } s_i(x) = -1 \\ 0 & \text{if } s_i(x) = 0, \end{cases} \quad (5)$$

where  $b_{\text{mag},i} \in \mathbb{R}$  is a shared magnitude offset and  $g_i^\pm = \exp(r_i^\pm) \geq 0$  are separate gains for positive and negative activations, with the exponent used to guarantee positive values.

Bi-Jump-ReLU is a signed dead-zone unit: it is identically zero inside  $[-\delta_i^-, \delta_i^+]$ , uses gain  $g_i^+$  on the positive side, and gain  $g_i^-$  on the negative side, while both polarities share the same decoder column. Unlike soft-thresholding or one-sided JumpReLU, thresholds decide support but are not subtracted from the active magnitude. Related two-sided thresholded units have appeared in other settings, including symmetric threshold-linear networks and symmetric-threshold ReLU constructions [25, 26]. Our novelty is the integration of this signed dead-zone behavior into a decoder-aligned gated SAE with shared signed decoder directions and the no-shrinkage support/magnitude separation of Gated SAEs.

#### 3.2 Training Objective

The decoder reconstructs as

$$\hat{x} = Da(x) + b_{\text{dec}}, \quad (6)$$

where  $a(x) \in \mathbb{R}^H$  collects the Bi-Jump-ReLU activations. We adapt the Gated SAE loss by placing sparsity pressure on the gate and using an auxiliary reconstruction to train detection separately from the magnitude path:

$$\mathcal{L}(x) = \underbrace{\|x - Da(x) - b_{\text{dec}}\|_2^2}_{\text{Main Reconstruction}} + \lambda \sum_i \Omega_{\text{gate}}(\pi_i(x)) + \lambda_{\text{aux}} \mathcal{L}_{\text{aux}}(x). \quad (7)$$

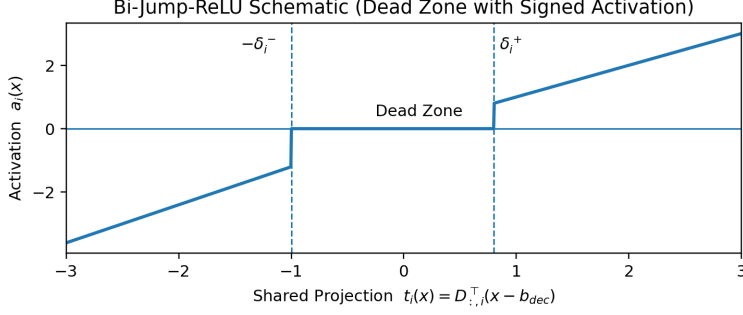


Figure 1: Bi-Jump-ReLU is zero inside a learnable dead zone  $[-\delta_i^-, \delta_i^+]$  and emits signed magnitude outside it, using one decoder direction for both polarities.

The gate penalty is a two-sided hinge,

$$\Omega_{\text{gate}}(\pi_i(x)) = \text{ReLU}(\pi_i(x) - \delta_i^+) + \text{ReLU}(-\pi_i(x) - \delta_i^-), \quad (8)$$

which is zero inside the dead zone and grows linearly outside it.

To supervise the gate directly, we use an auxiliary reconstruction with a stop-gradient decoder path,

$$\mathcal{L}_{\text{aux}}(x) = \|x - D^{\text{sg}}[\text{ReLU}(\pi(x) - \delta^+) - \text{ReLU}(-\pi(x) - \delta^-)] - b_{\text{dec}}^{\text{sg}}\|_2^2, \quad (9)$$

where  $D^{\text{sg}} := \text{stopgrad}(D)$  and  $b_{\text{dec}}^{\text{sg}} := \text{stopgrad}(b_{\text{dec}})$  are treated as constants for this term. This preserves the intended separation: the auxiliary objective teaches the gate which side of the dead zone to cross, while the main reconstruction learns the signed magnitude once a latent is active. Implementation details and effective-threshold analysis are deferred to Appendix B. LLM baseline definitions are summarized in §4.1.

### 3.3 Parameter Efficiency & Width Reduction

Suppose a baseline SAE has width  $H$ , and that a fraction  $p \in [0, 1]$  of the ground-truth features in the data representation appear as perfectly anticorrelated pairs aligned to directions  $\pm d$ . If there are  $N$  total ground-truth features, then  $pN$  of them participate in pairs, yielding  $(pN)/2$  pairs and  $(1-p)N$  unpaired features. A baseline SAE requires two latents for each pair, so it uses  $H = N$  latents in total.

The Sign-Aware model instead requires only one latent per anticorrelated pair, plus one latent for each unpaired feature. The effective width required for the Sign-Aware model is therefore

$$H_{\pm} = (1-p)N + \frac{pN}{2} = N \left(1 - \frac{p}{2}\right) = H \left(1 - \frac{p}{2}\right). \quad (10)$$

If  $p = 1$  (all features are paired), the dictionary size halves.

We now analyze the parameter overhead. Let  $d_{\text{in}}$  be the input dimensionality. In a standard Gated SAE, each latent carries roughly  $d_{\text{in}}$  parameters for the decoder direction plus  $O(1)$  scalar parameters for gate biases and scales; we summarize this as  $d_{\text{in}} + c$  parameters per latent for some small constant  $c$ . The Sign-Aware architecture adds 4 scalars per latent (two thresholds, two magnitude scales) compared to the standard Gated SAE, so per-latent parameters become  $d_{\text{in}} + c + 4$ .

Approximating the total parameter counts as

$$P_{\text{base}} \approx H(d_{\text{in}} + c), \quad (11)$$

$$P_{\text{sign}} \approx H_{\pm}(d_{\text{in}} + c + 4) = H \left(1 - \frac{p}{2}\right) (d_{\text{in}} + c + 4), \quad (12)$$

we obtain the condition for net parameter savings:

$$P_{\text{sign}} < P_{\text{base}} \implies \left(1 - \frac{p}{2}\right) (d_{\text{in}} + c + 4) < d_{\text{in}} + c \quad (13)$$

$$\implies 4 - \frac{p}{2}(d_{\text{in}} + c + 4) < 0 \quad (14)$$

$$\implies p > \frac{8}{d_{\text{in}} + c + 4}. \quad (15)$$

Taking  $c \approx 0$  for simplicity yields the approximate threshold

$$p \gtrsim \frac{8}{d_{\text{in}} + 4}. \tag{16}$$

At all six hookpoint  $\times$  backbone cells of our LLM benchmark the hookpoint activation dimension is  $d_{\text{in}} = 2048$  (both Pythia-1B and SmoLLM3-3B have hidden size 2048), so the threshold becomes  $p \gtrsim 8/2052 \approx 0.39\%$ . Under a simple parameter-counting model, the Sign-Aware SAE is therefore strictly parameter-efficient as soon as anticorrelated pairs constitute a small fraction of the feature set, on the order of  $10^{-3}$  for typical transformer-scale widths.

**Symmetric-magnitude variant.** A symmetric-magnitude variant that ties  $r_i^+ = r_i^-$ , reducing the per-latent scalar overhead by one, is discussed in Appendix B.

**Empirical lower bound on  $p$  at transformer hookpoints.** A direct test of the parameter-efficiency premise requires an observation of the fraction  $p$  of feature axes that admit sign-sharing in real activations. Since the ground-truth feature basis is not known, we use the proxy  $\hat{p} = \text{both\_fraction\_valid}$  – the fraction of trained SA-GSAE latents whose  $\gamma_+$  and  $\gamma_-$  are each individually identifiable from a held-out activation cache (each regime has  $\geq 32$  firing tokens with non-degenerate squared-activation mass). This is a lower bound on the true  $p$ : a latent is counted only if it has demonstrably fired with substantial magnitude on both signs. At matched  $L_0 = 64$  and  $d_{\text{in}} = 2048$  the theoretical threshold is  $p \gtrsim 0.39\%$ . The observed  $\hat{p}$  ranges from 0.039 (resid-mid/SmoLLM3-3B full-width) to 0.767 (mlp\_out-mid/SmoLLM3-3B half-width), clearing the theoretical threshold by  $10\times$  at the worst observed cell and by roughly  $200\times$  at the best (table 6). Sign-awareness is therefore parameter-efficient in practice, not merely in principle, across every benchmark cell we tested.

## 4 Results

All experiments, including failed runs, closed in approximately 4000 compute hours of AWS g5.2xlarge instances (NVIDIA A10G Tensor Core GPU) and 200 compute hours of AWS g4dn.xlarge instances (NVIDIA T4 GPU). Controlled synthetic and toy experiments are reported in Appendix C and Appendix D.

The licenses and date of verification of models and datasets are listed in Appendix H.

**Benchmark setup.** We cache token-level activations at three mid-depth hookpoints in each of two models: MLP output (mlp\_out), attention output (attn), and post-block residual stream (resid). The backbones are Pythia-1B at layer 8/16 [27] (pretrained on The Pile [28]) and SmoLLM3-3B at layer 18/36 [29]. Activations are collected on OpenWebText [30], using length-128 sequences with a fixed 90/5/5 train/val/test split. The cache uses 50k sequences per backbone with float16 precision.

We train width-32,768 SAEs (full width) and width-16,384 SAEs (half width) on the cached activations for each variant, holding the LLM frozen and using the same cache across all variants. Training runs in mixed precision at learning rate  $3 \cdot 10^{-4}$ ; Pythia uses batch size 256 for 31,250 steps and SmoLLM3 batch size 128 for 62,500 steps, with dead-latent resampling every 3906 and 7812 steps, respectively. For threshold/gated variants (Gated SAE, SA-GSAE) we sweep the sparsity coefficient  $\lambda$  over 8 log-spaced values; the exact per-method grid differs slightly, so we interpolate in  $\log L_0$  between adjacent sweep points when reporting matched-point quantities. For AbsTopK we train with  $k \in \{16, 32, 64, 128\}$ . All results report mean  $\pm$  SE over 3 random seeds. We report reconstruction MSE and  $R^2$ , mean  $L_0$ , dead-feature fraction, and Loss Recovered (LR), defined as the fraction of the clean-to-zero-ablation language-model loss gap recovered when the SAE reconstruction is patched back into the same hookpoint.

LR saturates at residual-stream hookpoints and has a noise-dominated ceiling on attn-mid/SmoLLM3-3B; we therefore treat  $R^2$  and MSE as primary discriminators there and do not compare LR across hookpoints.

**Comparison protocol and scope.** All LLM variants are trained in the same shared harness with matched width, activation cache, data split, seed count, and overall training budget. For continuous sweeps (Gated SAE, SA-GSAE), the matched-point tables linearly interpolate in  $\log L_0$  between

adjacent sweep points on each seed’s curve before aggregating; for AbsTopK we report the nearest fixed- $k$  anchor. The benchmark covers three mid-depth hookpoints per backbone and focuses on reconstruction/capacity metrics; it does not by itself establish downstream interpretability wins across layers or model families.

#### 4.1 Baseline Implementations for the LLM Benchmark

For real-LLM activation experiments, the main-text comparison uses Gated SAE and AbsTopK baselines implemented in the shared harness. We document the exact implementation details used in these runs:

- **Gated SAE:** we use the shared projection  $t_i(x) = D_{:,i}^\top(x - b_{\text{dec}})$ , gate pre-activation  $\pi_i(x) = \alpha_i t_i(x) + \beta_i$ , and activation

$$a_i(x) = \mathbf{1}[\pi_i(x) > 0] \text{ReLU}(g_i t_i(x) + b_{\text{mag},i}).$$

The sparsity source is  $\text{ReLU}(\pi_i(x))$ , and the baseline uses the standard frozen-decoder auxiliary reconstruction from [24].

- **AbsTopK SAE:** we keep signed pre-activations  $u_i(x)$ , apply deterministic per-sample top- $k$  selection on  $|u_i(x)|$  using detached scores, and set  $a_i(x) = m_i(x)u_i(x)$ .

AbsTopK uses fixed- $k$  sparsity control and therefore does not add an explicit sparsity-coefficient term to the reconstruction loss in these runs.

**Fairness note on encoder parameterization.** SA-GSAE and Gated SAE use the shared projection  $t_i(x) = D_{:,i}^\top(x - b_{\text{dec}})$ , whereas AbsTopK retains its native encoder parameterization in the shared harness. We intentionally keep each baseline in its standard, well-performing form rather than forcing a common encoder template, because the practical question is whether sign-aware gating is competitive with the methods practitioners actually use. The LLM tables should therefore be read as end-to-end recipe comparisons, not as a pure isolation of encoder tying versus untied encoders. The hybrid AbsTopK+GatedMag ablation in Appendix E partially disentangles this issue by pairing our magnitude path with a fixed- $k$  signed selector.

**Pareto frontiers: dead fraction vs  $L_0$ .** We plot the full  $\lambda$ -sweep dead-fraction frontier on each of the six hookpoint  $\times$  backbone cells in fig. 2; the per-cell Loss-Recovered companion is fig. 3, and the underlying sweep statistics are tabulated in table 7. Our top-level claim is curve-level rather than point-level: on every cell, the half-width SA-GSAE dead-fraction frontier lies at or below the full-width Gated SAE frontier over essentially the entire swept sparsity range, and on three of the six cells it does so while simultaneously matching or exceeding Gated-full  $R^2$  at every  $L_0$  in the overlap — strict Pareto-dominance. Those three cells are `mlp_out-mid/Pythia-1B` ( $L_0 \in [15.3, 144.4]$ ), `mlp_out-mid/SmolLM3-3B` ( $L_0 \in [5.4, 127.4]$ ), and `resid-mid/Pythia-1B` ( $L_0 \in [17.9, 129.3]$ ); on them the sweep-median dead-fraction reduction is  $155\times$ ,  $60\times$ , and  $191\times$  respectively (geometric means  $145\times$ ,  $96\times$ ,  $492\times$ ), with peak in-overlap absolute dead-fraction drops of  $0.626 \rightarrow 4.3 \cdot 10^{-5}$  on `resid-mid/Pythia-1B` at  $L_0 \approx 125$  (ratio  $1.5 \cdot 10^4\times$ ) and  $0.835 \rightarrow 8.4 \cdot 10^{-5}$  on `mlp_out-mid/SmolLM3-3B` at  $L_0 \approx 121$  ( $\Delta R^2 = +0.015$ ; ratio  $1.0 \cdot 10^4\times$ ). On the remaining three cells the dead-fraction ordering is still one-sided (SA-half dead  $\leq$  Gated-full dead at 100% of overlap on both attention cells and at 99.4% of overlap on `resid-mid/SmolLM3-3B`), but the  $R^2$  gap reverses slightly at high  $L_0$ : Gated SAE edges ahead by up to 0.011  $R^2$  on `attn-mid/Pythia-1B` and by up to 0.025  $R^2$  on `attn-mid/SmolLM3-3B`. Across all six cells  $\Delta R^2 \in [-0.008, +0.023]$  (signed; ties or exceeds Gated-full on 3/6 cells) over the entire overlap, and SA-half still strictly Pareto-dominates the low- $L_0$  region of both attention cells (up to  $L_0 \approx 23$  on Pythia-1B and  $L_0 \approx 39$  on SmolLM3-3B; extending to  $\approx 25$  and  $\approx 43$  once SA-half is permitted to match Gated-full  $R^2$  within the per-sweep-point standard error of  $10^{-3}$ ). On `resid-mid/SmolLM3-3B` the sweep-median and geometric-mean dead-fraction reductions are  $2.0\times$  and  $4.0\times$ . Two frontier-visible pathologies remain worth flagging: (i) on `mlp_out-mid/Pythia-1B` the full-width Gated SAE  $L_0$  curve is non-monotone in  $\lambda$  on 3/3 seeds (drops to  $\sim 14$  at  $\lambda \approx 3.1 \cdot 10^{-3}$ , rebounds to  $\sim 19$ – $21$ ), while full-width SA-GSAE is strictly decreasing in  $\lambda$  on 3/3 seeds – the  $L_0$ -reversal pathology belongs to Gated SAE, not SA-GSAE; (ii) on `resid-mid/SmolLM3-3B` the full-width SA-GSAE frontier exhibits a reproducible reconstruction collapse (MSE up to 6.0,  $R^2$  to  $-4.3$ , 3/24 sweep points with  $\text{LR} < 0.5$ , min  $\text{LR} = 0.175$ ) that the half-width variant entirely

avoids ( $R^2 \geq 0.985$ ,  $MSE \leq 0.018$ ); per-seed audit in section F and table 5. AbsTopK reaches effectively zero dead on MLP and residual hookpoints but is not a universally zero-dead baseline: on `attn-mid/Pythia-1B` it records 50.2% dead at  $k = 64$ , rising to 72.5% at  $k = 16$ .

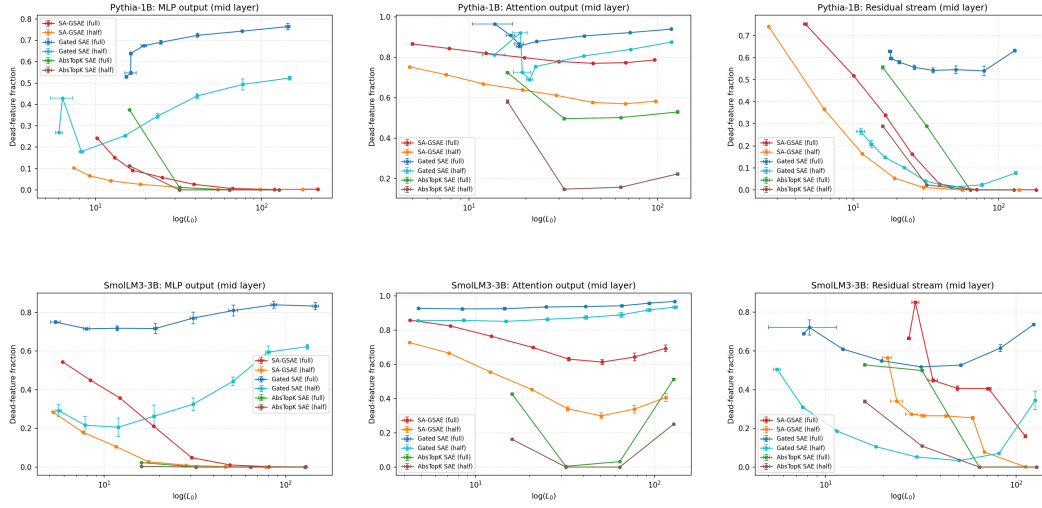


Figure 2: Dead-feature fraction vs  $\log(L_0)$  across the three mid-depth hookpoints (columns: `mlp_out`, `attn`, `resid`). Top row: Pythia-1B (layer 8/16). Bottom row: SmoLLM3-3B (layer 18/36). Error bars show  $\pm SE$  over 3 seeds on both axes.

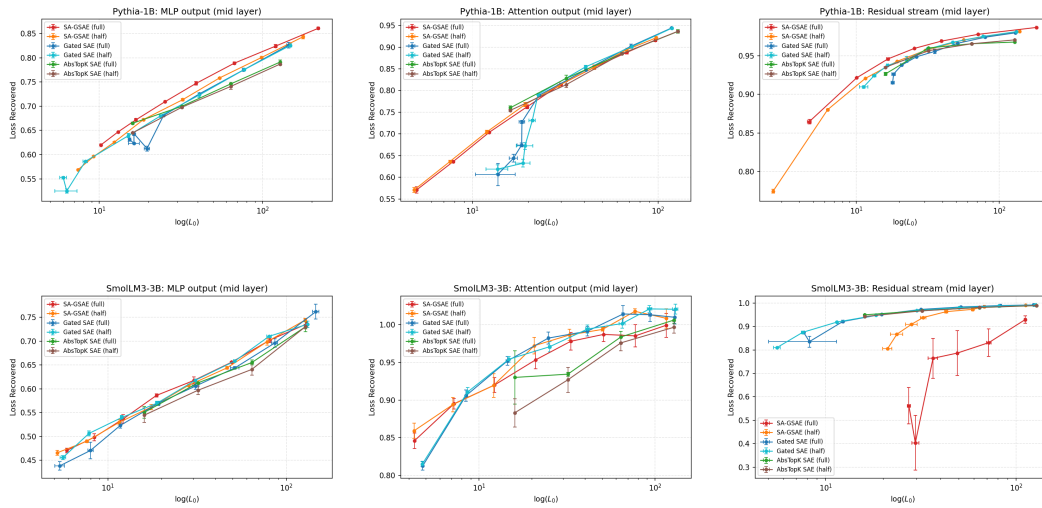


Figure 3: Loss Recovered (LR) vs  $\log(L_0)$  across the three mid-depth hookpoints (columns: `mlp_out`, `attn`, `resid`). Top row: Pythia-1B (layer 8/16). Bottom row: SmoLLM3-3B (layer 18/36). Error bars show  $\pm SE$  over 3 seeds on both axes. LR saturates near 1 at residual-stream hookpoints and has a noise-dominated ceiling on `attn/SmoLLM3-3B` (baseline gap 0.037 nats); see benchmark setup for the LR-not-cross-hookpoint-comparable caveat.

**Matched-LR crossings on MLP outputs.** LR is only discriminating on MLP-output cells (elsewhere it saturates; see benchmark setup). Reading fig. 3 as a family of frontiers rather than at a fixed  $L_0$ : on `mlp_out-mid/Pythia-1B` the SA-half curve crosses LR = 0.75 at  $L_0 = 50.4 \pm 0.6$ , MSE  $0.0418 \pm 0.0001$ , 0.4%  $\pm$  0.0% dead, whereas the Gated-full ( $2H$ ) curve crosses the same LR target at  $L_0 = 58.8 \pm 1.7$ , MSE  $0.0431 \pm 0.0002$ , 73.2%  $\pm$  0.6% dead. On `mlp_out-mid/SmoLLM3-3B` the

SA-GSAE family tops out near LR  $\approx 0.68$ ; at that common target, SA-half crosses at  $L_0 = 67.6 \pm 3.1$ , MSE  $0.00238 \pm 0.00003$ ,  $0.1\% \pm 0.0\%$  dead, versus Gated-full at  $L_0 = 77.0 \pm 3.4$ , MSE  $0.00243 \pm 0.00003$ ,  $83.0\% \pm 2.4\%$  dead.

**Calibration symmetry and bipolar-latent usage.** For each signed latent we fit split-regime slopes  $\gamma_+$ ,  $\gamma_-$  and report  $\hat{p} := \text{both\_fraction\_valid}$ , a calibration-based lower bound on the anticorrelation rate  $p$  of §3.3; full detail in tables 6 and 8 and sections G, G.2 and G.3. (i) On every cell, SA-GSAE medians of  $\gamma_+$  and  $\gamma_-$  agree within  $\leq 0.05$  and  $[p_{10}, p_{90}]$  intervals overlap almost exactly – direct real-activation evidence for the symmetric-magnitude default  $r_i^+ = r_i^-$  (ablation:  $|\Delta R^2| = 0.0015$ ,  $|\Delta \text{MSE}| = 0.0002$ , table 4). (ii) AbsTopK attains median  $\gamma \approx 1.00$  with  $[p_{10}, p_{90}] \approx [0.97, 1.03]$  on every cell; this follows mechanically from its lack of a learnable dead zone (the support-selection scale mismatch in section B cannot arise) and is not a calibration-training win. SA-GSAE’s  $\gamma_{\pm}$  medians of  $\approx 2\text{--}3$  reflect support-selection overshoot, not  $L_1$  shrinkage. (iii) Two bipolar statistics, two hookpoint patterns: dictionary-wide coverage  $\hat{p}$  concentrates on MLP outputs and resid-mid/Pythia-1B – SA-half  $\hat{p} = 0.767$  on mlp\_out-mid/SmolLM3-3B, 0.481 on resid-mid/Pythia-1B, 0.283 on mlp\_out-mid/Pythia-1B, versus 0.082–0.322 on attention and resid-mid/SmolLM3-3B (table 6) – exactly the cells where half-width SA-GSAE Pareto-dominates or ties Gated SAE (table 1); broad coverage drives the MLP-output capacity wins. Top-64 qualitative bipolar latents, by contrast, concentrate at attention: 12/64 (19%) on attn-mid/Pythia-1B, 3/64 on attn-mid/SmolLM3-3B, 5/64 on resid-mid/Pythia-1B, and 0–1 per file elsewhere (see section G.3 and table 9, including the Pythia attn latent 22641 contrasting “Parent Revolution” with Murdoch-owned-media tokens). The quantitative payoff is visible on the  $\gamma_+$ -valid/alive-fraction axis: SA-GSAE-full on mlp\_out-mid/Pythia-1B reaches  $0.651 \pm 0.002$ ,  $2.5\times$  Gated SAE’s  $0.264 \pm 0.004$ , and is preserved at  $0.642 \pm 0.001$  by SA-half.

## 4.2 Half-Width Validation: SA-GSAE at $H$ Matches Gated SAE at $2H$

The halved-width operating point is the natural regime for SA-GSAE: if each sign-aware latent carries double the information, the dictionary needs only half as many entries. We train SA-GSAE at  $H = 16,384$  and compare it to a Gated SAE at  $2H = 32,768$  on identical cached activations, with the same optimizer, training schedule, and evaluation protocol, on all six hookpoint  $\times$  backbone cells. Table 1 reports the resulting  $\Delta R^2$ ,  $\Delta \text{MSE}$ , and  $\Delta \text{Dead}$  (half-width SA-GSAE minus full-width Gated SAE) at matched  $L_0 = 64$ .

We separate two effects. (i) *Sign-awareness at matched width.* Against Gated SAE at the same width  $H$  (Gated-half), SA-half strictly Pareto-dominates on both mlp\_out-mid cells ( $\Delta R^2 = +0.017, +0.013$ ;  $\Delta \text{Dead} = -0.476, -0.518$ ) and effectively ties on resid-mid/Pythia-1B ( $\Delta R^2 = +0.0001$ ,  $\Delta \text{Dead} = -0.019$ ); it trades small  $R^2$  for substantial dead-fraction reductions on both attention cells ( $\Delta R^2 \in [-0.008, -0.006]$ ,  $\Delta \text{Dead} \in [-0.568, -0.262]$ ); and it is dominated by Gated-half only on resid-mid/SmolLM3-3B ( $\Delta R^2 = -0.002$ ,  $\Delta \text{Dead} = +0.102$ ). Thus sign-awareness – not width – drives the  $R^2$  and dead-fraction gains on the MLP-output cells. (ii) *Operational-budget comparison.* Against the nominally  $2\times$ -wider Gated-full, SA-half matches reconstruction with  $\Delta R^2 \in [-0.008, +0.023]$  (ties or exceeds on 3/6 cells; max negative gap  $-0.008$  on attn-mid/Pythia-1B) while cutting dead fraction by 0.35–0.82 absolute on all 6 cells. The halved-width operating-point recommendation is thus supported by both comparators jointly.

**Ablation summary.** Appendix E (table 4) isolates the design choices on Pythia-1B mlp\_out at matched  $L_0 = 64$ . Removing the auxiliary loss is catastrophic (LR = 0.27, dead = 98%,  $L_0$  clamps at  $\sim 2$ ). Tying  $r_i^+ = r_i^-$  is practically indistinguishable from the full model ( $|\Delta R^2| = 0.0015$ ,  $|\Delta \text{MSE}| = 0.0002$ ); corroborated by cell-wise  $\gamma_{\pm}$  symmetry (table 8), we recommend the *symmetric-magnitude variant* (§3.3) as the SA-GSAE default. The  $\delta_0$  sweep is U-shaped ( $\{10^{-3}, 10^{-2}\}$  harmful;  $\{0.5, 1.0\}$  neutral), and the Hybrid AbsTopK+gated-magnitude variant is dominated by full SA-GSAE (MSE 0.0400 vs. 0.0375, 40% vs. 0.8% dead).

## 5 Limitations

**Empirical scope.** Three hookpoints (mlp\_out-mid, attn-mid, resid-mid)  $\times$  two backbones (Pythia-1B, SmolLM3-3B)  $\times$  three seeds, at two widths. Layer sweeps, longer-context activations, RLHF’d / instruction-tuned backbones, and  $>3\text{B}$ -parameter models are out of scope. A width sweep

Table 1: Half-width validation at matched  $L_0 = 64$  (mean over 3 seeds;  $\pm$  SE shown on the Gated-full  $\Delta R^2$  column; Gated-half comparator SEs are comparable,  $\leq 0.002$ ). We compare half-width SA-GSAE ( $H = 16,384$ ) against both full-width Gated SAE ( $2H = 32,768$ , operational-budget comparison) and matched-width Gated SAE ( $H$ , which isolates sign-awareness) on every hookpoint  $\times$  backbone cell.

Backbone	Hookpoint	SA-half – Gated-full ( $2H$ )			SA-half – Gated-half ( $H$ )		
		$\Delta R^2$	$\Delta$ MSE	$\Delta$ Dead	$\Delta R^2$	$\Delta$ MSE	$\Delta$ Dead
Pythia-1B	mlp_out	$+0.016 \pm 0.001$	$-0.0024$	$-0.735$	$+0.017$	$-0.0025$	$-0.476$
	attn	$-0.008 \pm 0.001$	$+0.0003$	$-0.349$	$-0.008$	$+0.0004$	$-0.262$
	resid	$+0.0005 \pm 0.0000$	$-0.014$	$-0.543$	$+0.0001$	$-0.0023$	$-0.019$
SmolLM3-3B	mlp_out	$+0.022 \pm 0.005$	$-0.00010$	$-0.820$	$+0.013$	$-0.00007$	$-0.518$
	attn	$-0.007 \pm 0.001$	$+0.00002$	$-0.622$	$-0.006$	$+0.00002$	$-0.568$
	resid	$-0.001 \pm 0.001$	$+0.0008$	$-0.413$	$-0.002$	$+0.0025$	$+0.102$

down to  $H/4$  and below, which would test the parameter-efficiency prediction of §3.3 at tighter budgets, is a natural follow-up.

**Residual-stream LR saturation and cross-hookpoint incomparability.** On residual-stream cells the Gated-SAE Loss-Recovered baseline gap is large (6.6/8.6 nats vs. 0.037/0.123 nats on mlp\_out and attn), making LR arithmetically compressible above  $\sim 0.95$  and near-artifactual  $\text{LR} > 1$  values possible; we anchor residual-stream comparisons on dead fraction and  $R^2$  rather than LR.

**Residual-stream collapse at full width on SmolLM3-3B.** MSE up to 6.0,  $R^2$  to  $-4.3$ , 3/24 sweep points with  $\text{LR} < 0.5$  (table 5); the half-width SA-GSAE entirely avoids this pathology on the same cell. The SA-GSAE-specific warmup asymmetry disclosed in section B.1 is a plausible contributing factor; a matched-warmup ablation is a natural follow-up.

**Missing evaluation axes and baseline coverage.** No SAEbench-style probing or causal-intervention evaluation; reconstruction-capacity metrics only. Baselines exclude Switch and Matryoshka SAEs [31, 32]; sign-awareness targets sign splitting, not absorption or hedging [33, 34]. Paired-duplicate and feature-ablation diagnostics are deferred.

## 6 Conclusion

SA-GSAE is *two-sided gated sparsity with signed magnitude and auxiliary supervision*: ablations identify the gate and auxiliary reconstruction as load-bearing. Across 3 hookpoints  $\times$  2 backbones  $\times$  3 seeds, a half-width SA-GSAE at  $H$  cuts dead fraction by sweep-geomean factors of  $\sim 100\times$  to  $500\times$  on MLP-output cells and resid-mid/Pythia-1B and  $\sim 2\times$  to  $4\times$  on the remaining cells vs. a full-width Gated SAE at  $2H$ , matches  $R^2$  within 0.025 on every cell, and strictly Pareto-dominates over the full swept  $L_0$  overlap on both MLP-output cells and on resid-mid/Pythia-1B (3 of 6 cells). We recommend the *symmetric-magnitude* variant ( $r_i^+ = r_i^-$ ) at half width, which also avoids a reproducible resid-mid/SmolLM3-3B full-width collapse.

## References

- [1] Chris Olah. Mechanistic interpretability, variables, and the importance of interpretable bases. <https://www.transformer-circuits.pub/2022/mech-interp-essay>, 2022.
- [2] Chris Olah, Nick Cammarata, Ludwig Schubert, Gabriel Goh, Michael Petrov, and Shan Carter. Zoom in: An introduction to circuits. *Distill*, 2020. URL <https://distill.pub/2020/circuits/zoom-in/>.
- [3] Ashish Vaswani, Noam Shazeer, Niki Parmar, Jakob Uszkoreit, Llion Jones, Aidan N. Gomez, Lukasz Kaiser, and Illia Polosukhin. Attention is all you need. In *Advances in Neural Information Processing Systems*, 2017. URL <https://papers.neurips.cc/paper/7181-attention-is-all-you-need.pdf>.
- [4] Tolga Bolukbasi, Adam Pearce, Ann Yuan, Andy Coenen, Emily Reif, Fernanda Viégas, and Martin Wattenberg. An interpretability illusion for BERT. *arXiv preprint arXiv:2104.07143*, 2021.
- [5] Nelson Elhage et al. Toy models of superposition. *arXiv preprint arXiv:2209.10652*, 2022.
- [6] Kiho Park, Yo Joong Choe, and Victor Veitch. The linear representation hypothesis and the geometry of large language models. *arXiv preprint arXiv:2311.03658*, 2023.
- [7] Joshua Engels, Eric J. Michaud, Isaac Liao, Wes Gurnee, and Max Tegmark. Not all language model features are one-dimensionally linear. *arXiv preprint arXiv:2405.14860*, 2024.
- [8] Bruno A. Olshausen and David J. Field. Emergence of simple-cell receptive field properties by learning a sparse code for natural images. *Nature*, 381(6583):607–609, 1996.
- [9] Robert Tibshirani. Regression shrinkage and selection via the lasso. *Journal of the Royal Statistical Society: Series B (Methodological)*, 58(1):267–288, 1996.
- [10] Michal Aharon, Michael Elad, and Alfred Bruckstein. K-SVD: An algorithm for designing overcomplete dictionaries for sparse representation. *IEEE Transactions on Signal Processing*, 54(11):4311–4322, 2006.
- [11] Julien Mairal, Francis Bach, Jean Ponce, and Guillermo Sapiro. Online dictionary learning for sparse coding. In *Proceedings of the 26th International Conference on Machine Learning (ICML)*, pages 689–696, 2009.
- [12] Daniel D. Lee and H. Sebastian Seung. Learning the parts of objects by non-negative matrix factorization. *Nature*, 401(6755):788–791, 1999.
- [13] Karol Gregor and Yann LeCun. Learning fast approximations of sparse coding. In *Proceedings of the 27th International Conference on Machine Learning (ICML)*, pages 399–406, 2010.
- [14] Trenton Bricken et al. Towards monosemanticity: Decomposing language models with dictionary learning. <https://transformer-circuits.pub/2023/monosemantic-features/index.html>, 2023.
- [15] Hoagy Cunningham, Aidan Ewart, Logan Riggs, Robert Huben, and Lee Sharkey. Sparse autoencoders find highly interpretable features in language models. *arXiv preprint arXiv:2309.08600*, 2023.
- [16] Leo Gao, Tom Dupré la Tour, Henk Tillman, Gabriel Goh, Rajan Troll, Alec Radford, Ilya Sutskever, Jan Leike, and Jeffrey Wu. Scaling and evaluating sparse autoencoders. *arXiv preprint arXiv:2406.04093*, 2024. URL <https://cdn.openai.com/papers/sparse-autoencoders.pdf>.
- [17] Tom Lieberum et al. Gemma scope: Open sparse autoencoders everywhere all at once on gemma 2. *arXiv preprint arXiv:2408.05147*, 2024.
- [18] Zhengfu He et al. Llama scope: Extracting millions of features from llama-3.1-8b with sparse autoencoders. *arXiv preprint arXiv:2410.20526*, 2024.
- [19] Charles O’Neill, Alim Gumran, and David Klindt. Compute optimal inference and provable amortisation gap in sparse autoencoders. *arXiv preprint arXiv:2411.13117*, 2024.
- [20] Jingyi Cui, Qi Zhang, Yifei Wang, and Yisen Wang. On the limits of sparse autoencoders: A theoretical framework and reweighted remedy. *arXiv preprint arXiv:2506.15963*, 2025.
- [21] Patrick Leask, Bart Bussmann, Michael Pearce, Joseph Bloom, Curt Tigges, Noura Al Moubayed, Lee Sharkey, and Neel Nanda. Sparse autoencoders do not find canonical units of analysis. *arXiv preprint arXiv:2502.04878*, 2025.
- [22] Gonçalo Paulo and Nora Belrose. Sparse autoencoders trained on the same data learn different features. *arXiv preprint arXiv:2501.16615*, 2025.
- [23] Xudong Zhu, Mohammad Mahdi Khalili, and Zhihui Zhu. AbsTopK: Rethinking sparse autoencoders for bidirectional features. *arXiv preprint arXiv:2510.00404*, 2025.
- [24] Senthoran Rajamanoharan, Arthur Conmy, Lewis Smith, Tom Lieberum, Vikrant Varma, János Krámár, Rohin Shah, and Neel Nanda. Improving dictionary learning with gated sparse autoencoders. *arXiv preprint arXiv:2404.16014*, 2024.
- [25] Richard H. R. Hahnloser, H. Sebastian Seung, and Jean-Jacques Slotine. Permitted and forbidden sets in symmetric threshold-linear networks. *Neural Computation*, 15(3):621–638, 2003. doi: 10.1162/089976603321192103.
- [26] Jianing Han, Ziming Wang, Jiangrong Shen, and Huajin Tang. Symmetric-threshold ReLU for fast and nearly lossless ANN-SNN conversion. *Machine Intelligence Research*, 20(3):435–446, 2023. doi:

- 10.1007/s11633-022-1388-2.
- [27] Stella Biderman, Hailey Schoelkopf, Quentin Anthony, Herbie Bradley, Kyle O’Brien, Eric Hallahan, Mohammad Aflah Khan, Shivanshu Purohit, USVSN Sai Prashanth, Edward Raff, Aviya Skowron, Lintang Sutawika, and Oskar van der Wal. Pythia: A suite for analyzing large language models across training and scaling. In *Proceedings of the 40th International Conference on Machine Learning (ICML)*, pages 2397–2430, 2023. URL <https://proceedings.mlr.press/v202/biderman23a.html>.
  - [28] Leo Gao, Stella Biderman, Sid Black, Laurence Golding, Travis Hoppe, Charles Foster, Jason Phang, Horace He, Anish Thite, Noa Nabeshima, Shawn Presser, and Connor Leahy. The Pile: An 800gb dataset of diverse text for language modeling. *arXiv preprint arXiv:2101.00027*, 2020.
  - [29] Elie Bakouch et al. SmolLM3: smol, multilingual, long-context reasoner. <https://huggingface.co/blog/smolLM3>, 2025.
  - [30] Aaron Gokaslan, Vanya Cohen, Ellie Pavlick, and Stefanie Tellex. Openwebtext corpus. <http://SkyLion007.github.io/OpenWebTextCorpus>, 2019.
  - [31] Anish Mudide, Joshua Engels, Eric J. Michaud, Max Tegmark, and Christian Schroeder de Witt. Efficient dictionary learning with switch sparse autoencoders. *arXiv preprint arXiv:2410.08201*, 2024.
  - [32] Bart Bussmann, Noa Nabeshima, Adam Karvonen, and Neel Nanda. Learning multi-level features with matryoshka sparse autoencoders. *arXiv preprint arXiv:2503.17547*, 2025.
  - [33] David Chanin et al. A is for absorption: Studying feature splitting and absorption in sparse autoencoders. *arXiv preprint arXiv:2409.14507*, 2024.
  - [34] David Chanin et al. Feature hedging: Correlated features break narrow sparse autoencoders. *arXiv preprint arXiv:2505.11756*, 2025.
  - [35] Ingrid Daubechies, Michel Defrise, and Christine De Mol. An iterative thresholding algorithm for linear inverse problems with a sparsity constraint. *Communications on Pure and Applied Mathematics*, 57(11): 1413–1457, 2004. doi: 10.1002/cpa.20042.
  - [36] Amir Beck and Marc Teboulle. A fast iterative shrinkage-thresholding algorithm for linear inverse problems. *SIAM Journal on Imaging Sciences*, 2(1):183–202, 2009. doi: 10.1137/080716542. URL <https://www.tau.ac.il/~becka/FISTA.pdf>.
  - [37] Alireza Makhzani and Brendan Frey. k-Sparse autoencoders. *arXiv preprint arXiv:1312.5663*, 2013.
  - [38] Senthoran Rajamanoharan, Tom Lieberum, Nicolas Sonnerat, Arthur Conmy, Vikrant Varma, János Krámár, and Neel Nanda. Jumping ahead: Improving reconstruction fidelity with JumpReLU sparse autoencoders. *arXiv preprint arXiv:2407.14435*, 2024.
  - [39] Bart Bussmann, Patrick Leask, and Neel Nanda. BatchTopK sparse autoencoders. *arXiv preprint arXiv:2412.06410*, 2024.
  - [40] Adam Karvonen et al. SAEBench: A comprehensive benchmark for sparse autoencoders in language model interpretability. *arXiv preprint arXiv:2503.09532*, 2025.
  - [41] Gonçalo Paulo and Nora Belrose. Evaluating SAE interpretability without explanations. *arXiv preprint arXiv:2507.08473*, 2025.
  - [42] Adam Karvonen, Benjamin Wright, Can Rager, Rico Angell, Jannik Brinkmann, Logan Smith, Claudio Mayrink Verdun, David Bau, and Samuel Marks. Measuring progress in dictionary learning for language model interpretability with board game models. *arXiv preprint arXiv:2408.00113*, 2024.
  - [43] Aleksandar Makelov, George Lange, and Neel Nanda. Towards principled evaluations of sparse autoencoders for interpretability and control. *arXiv preprint arXiv:2405.08366*, 2024.
  - [44] Aaron J. Li, Suraj Srinivas, Usha Bhalla, and Himabindu Lakkaraju. Evaluating adversarial robustness of concept representations in sparse autoencoders. *arXiv preprint arXiv:2505.16004*, 2025.
  - [45] Diederik P. Kingma and Jimmy Ba. Adam: A method for stochastic optimization. *arXiv preprint arXiv:1412.6980*, 2014. URL <https://arxiv.org/abs/1412.6980>.

## A Background and Related Work

### A.1 Sparse autoencoders as amortized sparse inference

Solving eq. (1) exactly requires an inner optimization to infer  $z^{(n)}$  for each sample, often via proximal methods (for example, ISTA/FISTA [35, 36]) that implement repeated shrinkage steps. Autoencoder-based approaches amortize this inference: an encoder network  $f_\theta(x)$  predicts  $z$  in a single forward pass, and a decoder reconstructs  $\hat{x} = Dz + b$ . This “learned inference” view has a long history in sparse coding [13], and it becomes particularly attractive when the dataset is large and the dictionary is highly overcomplete ( $H \gg d_{in}$ ).

In the SAE setting used for mechanistic interpretability, the decoder is typically linear and the encoder is a linear map followed by a sparsifying nonlinearity. Popular choices include:

- ReLU with an  $L_1$  penalty on activations.
- Hard TopK masking, which keeps exactly  $k$  active latents per sample [37].

Recent work emphasizes that the training objective, the sparsity mechanism, and the normalization of decoder columns jointly determine the learned feature geometry [16].

### A.2 Sparsity mechanisms and the shrinkage problem

A core tension in SAE training is the sparsity-fidelity trade-off: increasing sparsity typically harms reconstruction. For  $L_1$ -regularized SAEs, the sparsity penalty biases the magnitudes of active latents downward, an effect often called shrinkage. This is not just a cosmetic issue: underestimating feature magnitudes can systematically distort the reconstructed activation and degrade downstream “loss recovered” metrics [16]. Practical SAE training therefore involves broader trade-offs around shrinkage, dead latents, and how sparsity is enforced. Recent work has accordingly explored gated objectives, thresholded activations, fixed- $k$  selection, and broader evaluation suites [24, 38–41].

Among these directions, Gated SAEs address shrinkage by decoupling deciding which latents are active from estimating their magnitudes [24]. Concretely, a gating path computes pre-activations  $\pi(x)$  that are penalized for sparsity, while a separate magnitude path produces activations without paying an  $L_1$  cost. This separation yields Pareto improvements in reconstruction at a fixed average sparsity and has become a common baseline in recent work [24, 40]. Other approaches modify the sparsity nonlinearity directly, for example JumpReLU to improve reconstruction fidelity at similar sparsity [38], or BatchTopK to relax fixed per-sample sparsity constraints [39]. Evaluation work likewise argues that these mechanisms should be compared across broader suites of reconstruction, interpretability, and utility metrics [40, 41]. In principle these ideas could be combined: Gated SAEs separate support from magnitude, threshold-learning methods sharpen support selection, BatchTopK changes population sparsity control, whereas our focus is whether opposite polarities must occupy separate latents at all.

### A.3 Non-negativity, bidirectional features, and sign-awareness

Most widely used SAE variants in interpretability impose non-negativity on activations, either explicitly (ReLU) or implicitly through their sparsity mechanism. This interacts poorly with concepts that naturally live on a signed axis, where both positive and negative evidence are meaningful. A common workaround is sign splitting: represent a signed coefficient with two non-negative latents corresponding to the positive and negative parts. However, sign splitting doubles dictionary usage for every bidirectional axis, and in the SAE setting it can fragment what would otherwise be a single coherent feature direction into two mutually exclusive units.

The literature has recently begun to address this limitation directly. [23] derive common SAE nonlinearities from proximal updates for sparse coding and argue that non-negativity is an unnecessary constraint for recovering bidirectional features; they propose AbsTopK, which selects latents by absolute magnitude to retain signed activations. Our work is complementary: rather than modifying the selection rule alone, we incorporate sign-awareness into the gated, no-shrinkage objective by designing a single latent that can gate and scale positive and negative evidence along a shared decoder direction.

Conceptually, Bi-Jump-ReLU is closer to a signed dead-zone unit than to a proximal shrinkage map. Related two-sided thresholded units also appear outside the SAE literature, for example in symmetric threshold-linear networks and more recent symmetric-threshold ReLU constructions [25, 26]. Our claim is not that a signed dead zone is new in the abstract, but that it can be combined with decoder-aligned projections, gated no-shrinkage training, and auxiliary support supervision to remove sign splitting in modern SAEs. Classical soft-thresholding subtracts a threshold from the coefficient magnitude once a feature is active, and symmetric thresholding rules typically use the same thresholded quantity to determine both support and amplitude [35, 36]. JumpReLU similarly couples a jump threshold to a one-sided active magnitude [38]. By contrast, our unit uses thresholds only to decide whether a latent fires, while a separate unpenalized path determines how strongly it contributes once active. This distinction is what lets us combine sign-awareness with the no-shrinkage logic of Gated SAEs.

#### A.4 Evaluating SAE feature dictionaries

Because ground-truth internal features are rarely available, SAE quality is often assessed using proxy metrics such as reconstruction error, sparsity ( $L_0$ ), and loss recovered [16]. Recent work argues that these proxies are necessary but insufficient, and introduces evaluations that tie feature quality to interpretability and control. Examples include controlled environments with ground-truth features [42], task-specific supervised dictionaries for comparison [43], robustness-focused evaluations [44], and multi-metric suites that emphasize trade-offs between interpretability, disentanglement, and practical interventions [40, 41]. Our experiments are designed to report standard sparsity-fidelity curves, but also to explicitly test whether sign-aware latents reduce redundancy for anticorrelated pairs without sacrificing interpretability.

## B Supplementary Theory and Method Details

### B.1 Training-hyperparameter asymmetry between SA-GSAE and Gated SAE

SA-GSAE uses a two-sided threshold warmup of 40,000 steps on Pythia-1B and 80,000 steps on SmoLLM3-3B. We have not run a matched-warmup ablation isolating its effect, and such an ablation is a natural follow-up tied to the `resid-mid/SmolLM3-3B` collapse discussion in Limitations and section F.

### B.2 Computational Complexity

**Inference.** By caching the projection  $t(x) = D^\top(x - b_{\text{dec}})$ , the forward pass requires only one matrix multiplication for the encoder, identical in structure to the baseline. The subsequent gating and Bi-Jump-ReLU activations operate elementwise over the reduced sign-aware width  $H_\pm = H(1 - p/2)$ , just as in the standard Gated SAE. Since  $H_\pm \leq H$ , the total inference FLOPs scale down by the factor  $(1 - \frac{p}{2})$  relative to a baseline with width  $H$ .

**Training.** The Gated SAE objective requires an additional decoder pass for the auxiliary loss. In a conventional implementation this roughly adds one extra forward/backward pass through the decoder per optimization step. Relative to a baseline SAE with the same target width, this increases decoder-side compute by a factor on the order of  $1.5\times$  (the exact factor depends on how encoder and decoder costs balance), and this factor is further reduced by the width multiplier  $(1 - \frac{p}{2})$  that we gain from exploiting anticorrelated pairs. In other words, training is modestly more expensive per update than a non-gated SAE with the same width, but yields a permanently smaller and faster dictionary at inference time.

### B.3 Why the Magnitude-Path ReLU Does Not Reintroduce Classical Shrinkage

A natural concern is that SA-GSAE contains two support-affecting nonlinearities: the two-sided gate on  $\pi_i(x)$  and the ReLU in the magnitude path. Together they define effective positive and negative support thresholds on the shared projection  $t_i(x)$ ; the explicit formulas appear below in the discussion of effective thresholds. The key point is what happens once a branch is active: on either sign,  $a_i(x)$  is affine in  $t_i(x)$ , and the sparsity penalty acts only on the gate, not on the active magnitude. So the extra ReLU can change which tokens activate, but it does not reintroduce the

subtractive bias term characteristic of soft-thresholding. This does not guarantee perfect calibration, because support selection can still be imperfect, but it clarifies the sense in which SA-GSAE preserves the no-shrinkage logic of gated SAEs.

#### B.4 Method Details

**Implementation note.** In our implementation, we stop gradients from the gate sparsity term and the auxiliary reconstruction from flowing into the decoder dictionary. Concretely, the gate logits use  $\pi_i(x) = \alpha_i \text{stopgrad}(t_i(x)) + \beta_i$ , and the auxiliary decoder path uses  $D^{\text{sg}}$  and  $b_{\text{dec}}^{\text{sg}}$  (a stop-gradient view of the current decoder and bias). Following standard SAE practice, decoder columns are renormalized during training; the shared projection  $t_i(x)$  and the auxiliary path therefore both use the current normalized decoder. For numerical stability we parameterize  $\alpha_i = \exp(\log \alpha_i)$  and  $g_i^\pm = \exp(r_i^\pm)$  and clamp the exponent inputs to a fixed range (e.g.,  $[-20, 20]$ ), and we enforce  $\delta_i^\pm \geq 0$  via a ReLU/softplus parameterization (we use ReLU in code). This preserves the intended separation: the auxiliary objective trains gate parameters without shaping the decoder geometry.

**Training dynamics:** The auxiliary reconstruction provides gradients only to the gate-related parameters ( $\alpha_i, \beta_i, \delta_i^+, \delta_i^-$ ) via  $\pi_i(x)$ , while  $D^{\text{sg}}$  (and  $b_{\text{dec}}^{\text{sg}}$ ) receive no gradients through  $\mathcal{L}_{\text{aux}}$ . The main reconstruction term updates both the decoder  $D$  and the magnitude parameters ( $r_i^+, r_i^-, b_{\text{mag},i}$ ) via the signed activations  $a_i(x)$ . This cleanly separates detection (learned through the auxiliary path and gate penalty) from magnitude estimation (learned through the main reconstruction), mirroring the no-shrinkage argument for Gated SAEs in the non-signed case.

**Support/magnitude separation and effective thresholds.** Because  $\alpha_i = \exp(\log \alpha_i) > 0$ , the positive branch can contribute only when both the gate and the magnitude path are active, i.e.,

$$t_i(x) > \max \left\{ \frac{\delta_i^+ - \beta_i}{\alpha_i}, -\frac{b_{\text{mag},i}}{g_i^+} \right\}.$$

Analogously, the negative branch can contribute only when

$$t_i(x) < \min \left\{ \frac{-\delta_i^- - \beta_i}{\alpha_i}, \frac{b_{\text{mag},i}}{g_i^-} \right\}.$$

Thus the gate thresholds and the magnitude-path ReLU jointly determine support. What they do not do is subtract from the active magnitude: once a branch is on,  $a_i(x)$  is affine in the shared projection  $t_i(x)$  with slope  $\pm g_i^\pm$ , and neither  $\delta_i^\pm$  nor the sparsity penalty appears in that slope. In this sense the extra ReLU can change which tokens activate, but it does not reintroduce the classical shrinkage effect of soft-thresholding, where the active coefficient itself is biased toward zero. Our calibration analyses in Protocol A and on real LLM activations are designed to test exactly this point.

**On learnable thresholds and degenerate solutions.** A trivial failure mode for two-sided hinge penalties is to “solve” the sparsity term by expanding the dead zone. In SA-GSAE this is not viable in isolation: when  $s_i(x) = 0$  we set  $a_i(x) = 0$ , so the magnitude path cannot contribute unless the gate crosses a threshold. Increasing  $\delta_i^\pm$  therefore tends to reduce reconstruction capacity unless compensated by shifting/scaling  $\pi_i(x)$  so that truly useful latents still cross their thresholds (in which case the hinge penalty depends on the threshold margins  $\pi_i(x) - \delta_i^+$  and  $-\pi_i(x) - \delta_i^-$  rather than the absolute sizes of  $\delta_i^\pm$ ). Accordingly, when analyzing trained models we focus on threshold margins and effective thresholds rather than raw  $\delta_i^\pm$  values.

**Symmetric-magnitude variant.** An ablation of our architecture ties the per-polarity magnitude scaling parameters ( $r_i^+ = r_i^-$ ), while retaining signed gating and asymmetric thresholds. In the parameter-counting model above, this reduces the per-latent scalar overhead by one, i.e., the per-latent count becomes  $d_{\text{in}} + c + 3$  instead of  $d_{\text{in}} + c + 4$ . Empirically, on Protocol A with the default generator settings (LogNormal positives vs. Exponential negatives,  $p_+ = 0.7$ ), tying magnitudes leaves reconstruction essentially unchanged and yields near-ideal split-regime calibration. At our main operating point ( $\lambda = 10^{-3}$ ; 16 seeds), the full model is marginally better calibrated on the positive regime, while the symmetric-magnitude variant is marginally better on the negative regime; both remain close to the ideal  $\gamma_\pm = 1$ . This indicates that the dominant gain comes from enabling signed activations along a shared decoder direction, with independent per-polarity scaling acting as a small second-order refinement.

## C Experimental Protocols

We evaluate sign-awareness on three fronts:

1. asymmetric signed-axis calibration,
2. directional anomaly detection under a strict latent budget,
3. consolidation of anticorrelated pairs in toy geometry.

Unless otherwise stated, we report not only a single operating point, but also sparsity-fidelity trade-offs by sweeping the sparsity strength (e.g.,  $\lambda$ ) and plotting reconstruction MSE versus average  $L_0$  (active latents per example).

### C.1 Protocol A: The "Polarity Dial" (Asymmetry & Calibration)

Protocol A is a controlled synthetic setting where each ground-truth feature is a signed scalar coefficient along a random axis  $u_j \in \mathbb{R}^d$ . It tests whether an SAE can represent and calibrate both positive and negative evidence along the same axis without duplicating decoder atoms. For non-negative SAEs, this requires paired atoms  $(+u_j, -u_j)$ ; a sign-aware latent can represent both directions with one decoder column and a signed activation.

**Data generation.** We construct a synthetic dataset  $X \subset \mathbb{R}^d$  consisting of  $k$  axes aligned to random directions  $u_j \in \mathbb{R}^d$ . Each axis is active with probability  $\rho$ . If active, its sign  $s_j \in \{-1, +1\}$  is sampled from a Bernoulli distribution with parameter  $p_+$ , and the magnitude follows different distributions conditioned on the sign:

$$m_j \mid (s_j = +1) \sim \text{LogNormal}(\mu = 0, \sigma = 0.5), \quad (17)$$

$$m_j \mid (s_j = -1) \sim \text{Exponential}(\lambda = 1.5). \quad (18)$$

We deliberately use different positive and negative magnitude laws to break sign symmetry. The LogNormal positive branch creates broader, heavier-tailed magnitudes, while the Exponential negative branch keeps the opposite sign more concentrated near zero. The aim is to test whether one latent can share a decoder direction even when the two signs have different scale statistics, not just different frequencies. The input is

$$x = \sum_j s_j m_j u_j + \epsilon, \quad (19)$$

with small isotropic noise  $\epsilon$ .

**Baselines and ablations.** We compare the following model families:

- **Sign-Aware Gated SAE (ours):** Signed latents with two-tailed gating (a learnable dead zone) and the gated objective to avoid shrinkage.
- **Sign-Aware, symmetric magnitude (ablation):** The same model, but with tied per-polarity magnitude scales ( $r_i^+ = r_i^-$ ). This tests whether independent per-polarity scaling is necessary in practice, and provides a more parameter-efficient variant.
- **Standard Gated SAE (non-negative, width  $H$ ):** A conventional gated SAE with ReLU latents.
- **Standard Gated SAE (non-negative, width  $2H$ ):** The same gated SAE trained at  $2\times$  width. This controls for the representational requirement that non-negative models need paired atoms  $(+u_j, -u_j)$  to represent a signed axis.
- **Baseline ReLU SAE (width  $H$ ):** A standard SAE with ReLU latents.
- **Baseline ReLU SAE (width  $2H$ ):** The same ReLU SAE trained at  $2\times$  width.
- **Signed Soft-Threshold SAE (signed-latent baseline):** A signed-latent baseline using a soft-threshold nonlinearity (a standard choice in signed sparse coding). This baseline can represent negative coefficients without paired atoms, but exhibits the classical  $L_1$  shrinkage trade-off between sparsity and coefficient bias (and can become dense at low  $\lambda$ ), separating "signed latents" from the gated no-shrinkage objective.

**Axis-aware alignment and pairing.** To compare learned representations to ground-truth axes  $u_j$ , we evaluate at the axis level rather than treating  $u_j$  and  $-u_j$  as distinct targets. We normalize decoder columns to unit norm for alignment, then compute signed cosine similarities

$$s_{ij} = \cos(D_{:,i}, u_j),$$

and define an axis similarity score  $|s_{ij}|$ . For sign-aware (signed-latent) models, we perform a one-to-one matching between latents  $i$  and axes  $j$  via the Hungarian algorithm on the absolute similarities  $|s_{ij}|$ , and we record the sign of  $s_{ij}$  for diagnostics. For non-negative baselines, we additionally allow two latents to represent one axis: for each axis  $j$ , we select the best positively aligned latent  $i^+(j) = \arg \max_i s_{ij}$  and the best negatively aligned latent  $i^-(j) = \arg \min_i s_{ij}$  (subject to an alignment threshold). This credits baselines that learn paired atoms  $(+u_j, -u_j)$ , which is the expected mechanism by which non-negative models represent signed structure.

**Metrics.** We focus on *Split-Scale Calibration* at the axis level. For each ground-truth axis  $j$ , let

$$c_j(x) = s_j m_j \tag{20}$$

denote the ground-truth scalar coefficient along  $u_j$  in the generative model. We define the model’s scalar coefficient estimate  $\hat{c}_j(x)$  by projecting the relevant reconstructed contribution(s) onto  $u_j$ . For sign-aware (signed-latent) models with a single matched latent  $i(j)$ , we use

$$\hat{c}_j(x) = u_j^\top (a_{i(j)}(x) D_{:,i(j)}). \tag{21}$$

For non-negative baselines using paired atoms  $(i^+(j), i^-(j))$ , we use an axis-aggregated estimate

$$\hat{c}_j(x) = u_j^\top (a_{i^+(j)}(x) D_{:,i^+(j)} + a_{i^-(j)}(x) D_{:,i^-(j)}), \tag{22}$$

which reduces to  $\hat{c}_j(x) \approx a_{i^+(j)}(x) - a_{i^-(j)}(x)$  when  $D_{:,i^+(j)} \approx u_j$  and  $D_{:,i^-(j)} \approx -u_j$ . We then compute separate least-squares rescaling factors for the positive and negative halves of the data:

$$\gamma_+ = \arg \min_{\alpha} \mathbb{E}[(\alpha \hat{c}_j(x) - c_j(x))^2 \mid c_j(x) > 0], \tag{23}$$

$$\gamma_- = \arg \min_{\alpha} \mathbb{E}[(\alpha \hat{c}_j(x) - c_j(x))^2 \mid c_j(x) < 0]. \tag{24}$$

- **Ideal outcome:**  $\gamma_+ \approx 1$  and  $\gamma_- \approx 1$ .
- **Primary hypothesis:** The Sign-Aware Gated SAE achieves  $\gamma_+ \approx 1$  and  $\gamma_- \approx 1$  using one latent per axis at width  $H$ . Non-negative models can approach this only if they allocate paired atoms; the  $2H$  baselines test whether remaining gaps at width  $H$  are primarily representational (insufficient atoms) rather than optimization-related.
- **Secondary question:** Whether independent per-polarity magnitude scaling ( $r_i^+ \neq r_i^-$ ) yields additional calibration gains beyond sign-awareness, tested via the symmetric-magnitude ablation.
- **Robustness diagnostics:** Because  $\gamma_{\pm}$  can become ill-conditioned when  $\hat{c}_j(x)$  collapses toward zero on a regime, we also report per-regime coefficient-space MSE, Pearson correlation between  $\hat{c}_j(x)$  and  $c_j(x)$ , and explained variance ( $R^2$ ), each computed separately on  $\{c_j(x) > 0\}$  and  $\{c_j(x) < 0\}$ .

## C.2 Protocol B: Directional Deviation Detection (Resource Constrained)

In control systems and operations monitoring, deviations often carry directional semantics (e.g., “pressure too high” vs. “pressure too low”). Protocol B benchmarks the Sign-Aware Gated SAE as a direction-aware anomaly detector under a strict latent budget constraint, and clarifies when such detection is feasible or fundamentally limited.

**Setup.** We simulate a high-dimensional sensor array  $x \in \mathbb{R}^N$  with  $N = 1024$  channels. We train models under a strict latent budget constraint  $H < N$  and evaluate detection at a fixed false positive rate (FPR).

**Normal distributions.** We consider two normal regimes:

- **Isotropic normal:**  $x \sim \mathcal{N}(0, I)$ .
- **Mildly heteroskedastic normal:**  $x_j \sim \mathcal{N}(0, \sigma_j^2)$  with distinct  $\sigma_j$  values close to 1. This breaks rotational symmetry while keeping channels approximately comparable, and is intended to make axis semantics learnable without strongly reweighting the reconstruction objective.

**Anomalies.** We evaluate two anomaly families:

- **Coordinate (channel) anomalies:** choose a channel  $j$  and shift  $x_j \mapsto x_j \pm \Delta$ .
- **Feature-direction anomalies:** choose a direction  $v_k \in \mathbb{R}^N$  and shift  $x \mapsto x \pm \Delta_k v_k$ .

For feature-direction anomalies, directions  $v_k$  are derived from a reference Sign-Aware model trained on the same normal data. We select the top- $M$  directions by the empirical standard deviation of the reference model’s detection signal (gate preactivation) on a clean normal split, which prioritizes directions that produce a strong gate signal. To reduce width-dependent effects, we optionally scale the input perturbation per direction using a fixed- $\Delta\pi$  rule:

$$\Delta_k = \frac{\Delta}{\alpha_k + \epsilon}, \quad (25)$$

where  $\alpha_k$  is the reference model’s per-latent gate scale for the selected latent and  $\epsilon$  is a small stabilizer. This targets an approximately constant first-order shift in the reference latent’s gate preactivation across selected directions.

**Directional scoring and calibration.** For the Sign-Aware model, let  $\pi_i(x)$  denote the gate preactivation of latent  $i$ . We optionally normalize the per-latent signal on validation normals to improve robustness under heteroskedastic or heavy-tailed normals:

$$\tilde{\pi}_i(x) = \frac{\pi_i(x) - \mu_i}{\max(\sigma_i, \epsilon)}, \quad (26)$$

where  $(\mu_i, \sigma_i)$  are fitted on validation normals and  $\epsilon$  is a small floor. We then define threshold margins for the positive and negative tails:

$$z_i^+(x) = \text{ReLU}(\tilde{\pi}_i(x) - \tau_i^+), \quad z_i^-(x) = \text{ReLU}(-\tilde{\pi}_i(x) - \tau_i^-), \quad (27)$$

where  $\tau_i^+$  and  $\tau_i^-$  are per-latent thresholds (e.g., the 99th percentile of  $\tilde{\pi}_i(x)$  and  $-\tilde{\pi}_i(x)$  on validation normals). We pool these threshold margins across latents to form directional anomaly scores:

$$\text{Score}_{\text{high}}(x) = \text{Pool}_i [z_i^+(x)], \quad \text{Score}_{\text{low}}(x) = \text{Pool}_i [z_i^-(x)], \quad (28)$$

where Pool is a configurable aggregation (sum, max, or top- $k$  sum). We choose score thresholds  $\theta_{\text{high}}$  and  $\theta_{\text{low}}$  to achieve a target FPR (1%) on validation normals, and report recall on held-out anomalies.

**Baselines and leakage prevention.** For baselines with non-negative activations, we use one-sided evidence signals and restrict directional scoring to avoid “two-sided leakage” from a single latent. Direction assignment uses decoder geometry (e.g., the sign of the dominant decoder component) and scoring pools threshold margins within the assigned direction group.

**Metrics.** We report:

- **Directional Recall at Fixed FPR:** recall for high and low anomalies at 1% FPR.
- **Coverage:** the fraction of targets for which both-direction recall exceeds a preset threshold (default 0.8). Targets are channels for coordinate anomalies and directions for feature-direction anomalies.
- **Alignment diagnostics:** decoder channel-purity and the number of unique channels claimed by latents (argmax channel occupancy), used to detect random-rotation behavior and quantify axis alignment.

**Protocol variants and expectations.** Under isotropic normals, coordinate anomalies serve as a non-identifiability control. Under mild heteroskedasticity, they test whether channel semantics emerge under strict compression. The main positive setting is feature-direction anomalies with strength control and localized pooling.

### C.3 Protocol C: Geometric Validation on Toy Models

We use a geometry-first toy-model validation suite that makes the anticorrelated pair consolidation behavior visually explicit in a controlled low-dimensional setting. Following [5], we generate  $k$  antipodal feature pairs in  $\mathbb{R}^2$  and train:

- a non-negative baseline at width  $M = 2k$ ;
- a Sign-Aware SAE at width  $M = k$  (with an optional overcomplete Sign-Aware variant at  $M = 2k$ ).

Protocol C includes:

- **Unit-circle geometry:** plot decoder directions against the ground-truth antipodal directions.
- **Bi-jump histogram:** plot the activation histogram for a representative sign-aware latent to visualize signed pair membership.
- **Superposition sweep:** vary the number of active pairs per sample  $n_{\text{active}}$  and measure signed recoverability as well as a thresholded Pair Consolidation Rate.
- **Robustness sweep:** vary within-pair correlation  $\rho \in [-1, 0]$  at fixed  $n_{\text{active}} = 1$ .

## D Results for Protocols A-C

This appendix reports controlled results for asymmetric signed-axis calibration (Protocol A), two-tailed directional detection under strict compression (Protocol B), and antipodal-pair consolidation in toy models (Protocol C). Experiments for Protocols A-C closed in approximately 60 compute hours of AWS g4dn.xlarge instances (NVIDIA T4 GPU).

### D.1 Protocol A: Asymmetry and Split-Scale Calibration

**Setup.** We evaluate Protocol A on the synthetic signed-axis dataset described in §C.1 with  $d = 512$  input dimensions and  $k = 128$  ground-truth axes. Each axis is active with probability  $\rho = 0.05$  and, when active, takes a positive sign with probability  $p_+ = 0.7$  and a negative sign otherwise. Conditional on sign, magnitudes are drawn from a LogNormal( $\mu = 0, \sigma = 0.5$ ) distribution for positives and an Exponential( $\lambda = 1.5$ ) distribution for negatives, with additive isotropic noise  $\epsilon \sim \mathcal{N}(0, 0.1^2 I)$ . We generate 200k training samples, 20k validation samples, and 20k test samples. All models are trained for 50 epochs with Adam [45] (learning rate  $10^{-4}$ ,  $\beta = (0.9, 0.999)$ ) and batch size 1024. We sweep the sparsity coefficient  $\lambda$  over 64 log-spaced values in  $[10^{-5}, 10^{-2}]$ ; the table below reports a representative sparse operating point at  $\lambda = 10^{-3}$ . We report mean  $\pm$  standard deviation over 16 random seeds (0-15), except for the Signed Soft-Threshold baseline, which uses the corrected implementation and is aggregated over 8 seeds (0-7) (marked † in table 2).

**Evaluation protocol.** We evaluate calibration at the axis level using the alignment and aggregation procedure in §C.1. Concretely, we match axes using absolute cosine similarity between decoder columns and ground-truth directions, with a minimum alignment threshold of  $\tau = 0.9$ . For non-negative baselines, we use the paired-atom aggregation  $\hat{c}_j(x)$  when both a positively aligned and negatively aligned latent are available for a given axis. This gives non-negative models credit for the intended representation  $(+u_j, -u_j)$  and ensures the comparison is not biased against baselines by the evaluation metric. Across the sparsity sweep, we find that axis matching under the strict threshold  $\tau = 0.9$  can degrade when sparsity pressure is too weak (consistent with rotational non-identifiability); we therefore focus our main conclusions on the sparse regime where axes are reliably matched.

Table 2: Protocol A results at  $\lambda = 10^{-3}$  (mean  $\pm$  std).  $H$  denotes the SAE width.  $L_0$  denotes the average number of non-zero latents per example.  $\bar{\gamma}_{\pm}$  is the mean split-regime calibration slope across axes, and  $\mathbb{E}[|\gamma_{\pm} - 1|]$  is the mean absolute slope error (lower is better). Non-negative baselines are evaluated with axis-level aggregation that credits paired atoms ( $+u_j, -u_j$ ) when present (§C.1). All rows use 16 seeds (0-15) except Signed Soft-Threshold ( $\dagger$ ), which uses the corrected implementation and is aggregated over 8 seeds (0-7).

Model	MSE $\downarrow$	$L_0 \downarrow$
ReLU SAE ( $H = 128$ )	0.018035 $\pm$ 0.001097	6.60 $\pm$ 0.33
ReLU SAE ( $H = 256$ )	0.017257 $\pm$ 0.000587	7.08 $\pm$ 0.64
Gated SAE ( $H = 128$ )	0.012981 $\pm$ 0.000047	9.36 $\pm$ 0.35
Gated SAE ( $H = 256$ )	<b>0.009956 <math>\pm</math> 0.000008</b>	9.22 $\pm$ 0.11
Signed Soft-Threshold SAE $^\dagger$ ( $H = 128$ )	0.011087 $\pm$ 0.000006	8.84 $\pm$ 0.04
Sign-Aware Gated SAE ( $H = 128$ )	0.009963 $\pm$ 0.000007	9.20 $\pm$ 0.07
Sign-Aware Gated SAE, symmetric magnitude ( $H = 128$ )	0.009964 $\pm$ 0.000007	9.20 $\pm$ 0.09

Model	$\bar{\gamma}_+$	$\bar{\gamma}_-$
ReLU SAE ( $H = 128$ )	0.773 $\pm$ 0.103	-1.554 $\pm$ 1.174
ReLU SAE ( $H = 256$ )	0.889 $\pm$ 0.055	-2.087 $\pm$ 1.563
Gated SAE ( $H = 128$ )	0.588 $\pm$ 0.063	-0.051 $\pm$ 0.011
Gated SAE ( $H = 256$ )	1.017 $\pm$ 0.018	1.037 $\pm$ 0.018
Signed Soft-Threshold SAE $^\dagger$ ( $H = 128$ )	1.243 $\pm$ 0.001	1.256 $\pm$ 0.002
Sign-Aware Gated SAE ( $H = 128$ )	1.039 $\pm$ 0.006	1.055 $\pm$ 0.005
Sign-Aware Gated SAE, symmetric magnitude ( $H = 128$ )	1.042 $\pm$ 0.005	1.041 $\pm$ 0.005

Model	$\mathbb{E}[ \gamma_+ - 1 ] \downarrow$	$\mathbb{E}[ \gamma_- - 1 ] \downarrow$
ReLU SAE ( $H = 128$ )	0.504 $\pm$ 0.064	2.558 $\pm$ 1.175
ReLU SAE ( $H = 256$ )	0.426 $\pm$ 0.037	3.089 $\pm$ 1.562
Gated SAE ( $H = 128$ )	0.440 $\pm$ 0.061	1.051 $\pm$ 0.011
Gated SAE ( $H = 256$ )	0.050 $\pm$ 0.017	0.070 $\pm$ 0.017
Signed Soft-Threshold SAE $^\dagger$ ( $H = 128$ )	0.243 $\pm$ 0.001	0.256 $\pm$ 0.002
Sign-Aware Gated SAE ( $H = 128$ )	<b>0.039 <math>\pm</math> 0.006</b>	0.055 $\pm$ 0.005
Sign-Aware Gated SAE, symmetric magnitude ( $H = 128$ )	0.042 $\pm$ 0.005	<b>0.041 <math>\pm</math> 0.005</b>

**Metrics.** We report reconstruction MSE on the test set, the average number of non-zero latents per example ( $L_0$ ), and split-regime calibration slopes  $\gamma_+$  and  $\gamma_-$  together with their mean absolute errors. Because  $\gamma_{\pm}$  can become unstable when a model collapses  $\hat{c}_j(x)$  toward zero on one regime, we additionally compute per-regime coefficient-space MSE, Pearson correlation, and  $R^2$ ; these diagnostics support the same conclusions and are included in the released artifacts.

Figure 4 shows the full sparsity sweep, making explicit that the sign-aware model matches the  $2\times$  width non-negative gated baseline across a broad  $L_0$  range while maintaining low two-tailed calibration error.

**The gap comes from needing two non-negative latents per signed axis, and sign-awareness closes it.** At width  $H = 128$ , non-negative models cannot allocate paired atoms ( $+u_j, -u_j$ ) for all axes, and the deficit shows up as a systematic failure to calibrate one side of the distribution. The standard Gated SAE achieves moderate positive-side calibration ( $\bar{\gamma}_+ \approx 0.59$ ) but collapses the negative side ( $\bar{\gamma}_- \approx -0.05$ ), yielding a large negative-regime slope error ( $\mathbb{E}[|\gamma_- - 1|] \approx 1.05$ ). The ReLU SAE baselines perform substantially worse, reflecting both the same non-negativity constraint and shrinkage under the standard  $L_1$  objective.

When we double the width of the non-negative Gated SAE to  $H = 256$ , it can represent each signed axis with two latents and recovers near-ideal calibration on both regimes ( $\bar{\gamma}_+ \approx 1.02$ ,  $\bar{\gamma}_- \approx 1.04$ ). At width  $H = 128$ , the Sign-Aware Gated SAE reaches comparable calibration quality using one latent per axis, while also achieving slightly lower mean absolute slope errors at this operating point. Its reconstruction error (0.009963) is within 0.1% of the  $H = 256$  non-negative gated baseline (0.009956), despite using half the dictionary width. This resolves the anticorrelation efficiency gap in the intended sense.

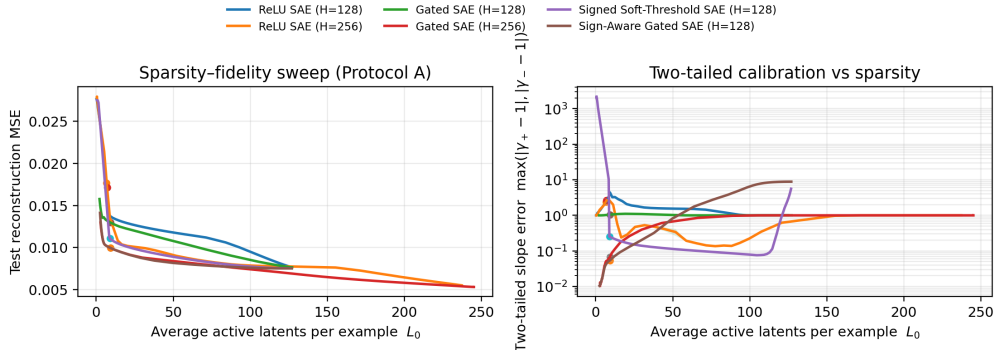


Figure 4: Protocol A (Polarity Dial) across the full sparsity sweep. Left: reconstruction MSE vs. average  $L_0$ . Right: two-tailed split-regime calibration error  $\max(|\gamma_+ - 1|, |\gamma_- - 1|)$  (log-scale y-axis) vs.  $L_0$ . Markers highlight the operating point  $\lambda = 10^{-3}$  used in Table 2. Shaded bands show  $\pm$ SE over seeds.

**Signed activations alone are not sufficient without the gated objective.** The Signed Soft-Threshold SAE can represent negative coefficients without paired atoms and, with the corrected implementation, can be tuned to match the sparsity of the gated models (e.g.  $L_0 \approx 8.8$  at  $\lambda = 10^{-3}$ ; table 2, †). However, it exhibits the classical  $L_1$  shrinkage bias: at this sparse operating point its split-regime slopes deviate systematically from the ideal value 1 ( $\bar{\gamma}_+ \approx 1.24$ ,  $\bar{\gamma}_- \approx 1.26$ ), yielding substantially larger mean absolute slope error than the gated no-shrinkage models. Coefficient-space diagnostics show high correlation but degraded scale accuracy, and reconstruction remains worse than the sign-aware and  $2\times$  width gated baselines at comparable sparsity. Across the  $\lambda$  sweep, soft-threshold exhibits a pronounced sparsity-bias trade-off: calibration improves in dense regimes, but degrades as  $\lambda$  increases; moreover, we observe a sharp instability/collapse for slightly larger  $\lambda$  as many axes become nearly inactive. This supports the motivation for combining sign-awareness with the gated no-shrinkage training objective rather than adopting signed sparse coding activations in an otherwise standard SAE.

**Independent  $r^+$ ,  $r^-$  scaling is not a dominant factor at these settings.** Tying the per-polarity magnitude scales ( $r_i^+ = r_i^-$ ) leaves reconstruction essentially unchanged and maintains near-ideal split-regime calibration. Under the default (asymmetric) Protocol A generator, we observe a small but consistent trade-off: the full model is marginally better calibrated on the positive regime (lower  $\mathbb{E}[|\gamma_+ - 1|]$ ), while the symmetric-magnitude variant is marginally better on the negative regime (lower  $\mathbb{E}[|\gamma_- - 1|]$ ). Overall, these differences are minor compared to the gap between sign-aware and non-sign-aware baselines, suggesting that independent per-polarity scaling is a second-order refinement rather than the primary driver of the Protocol A gains. Accordingly, the symmetric-magnitude variant is a reasonable default when prioritizing parameter minimality, while retaining the full model as a strictly more expressive option for settings with more extreme sign-conditioned asymmetry.

## D.2 Protocol B: Directional Deviation Detection

**Coordinate anomalies on isotropic normals are undetectable under strict compression.** On isotropic normals  $x \sim \mathcal{N}(0, I)$  with single-channel shifts, all evaluated models achieve directional recall close to the calibrated FPR (roughly 1% to 2% recall at 1% FPR) and 0 coverage across widths  $H \in \{32, 64, 128, 256, 512\}$ . Decoder alignment diagnostics are consistent with a random-rotation regime (low channel-purity and argmax-channel occupancy matching random assignment). This matches the expected non-identifiability: when the normal distribution is rotationally symmetric, no coordinate system is preferred, so single-channel shifts do not consistently create large per-latent tail events in the learned basis.

**Symmetry-breaking improves alignment but does not rescue coordinate monitoring.** We next break rotational symmetry using heteroskedastic normals with distinct channel variances, and enable per-latent z-score normalization and max pooling. While alignment diagnostics shift in the expected

Table 3: Protocol B results for feature-direction anomalies (mean over 16 seeds, target FPR 1%). Directions:  $M = 128$  selected by top-std( $\pi$ ) from a reference Sign-Aware model; per-direction inputs scaled by a fixed- $\Delta\pi$  rule and gate signals z-scored on validation normals before thresholding/pooling. Coverage denotes the fraction of directions with both-direction recall  $\geq 0.8$ .

Width $H$	Pooling	Sign-Aware Recall (high)	Sign-Aware Recall (low)	Coverage
128	max	0.999	0.999	1.00
256	max	0.998	0.999	1.00
512	max	0.998	0.998	1.00
512	top- $k$ ( $k = 4$ )	0.971	0.970	1.00

direction (higher decoder channel-purity and non-random argmax-channel occupancy), directional recall remains near the calibrated FPR and coverage remains 0 across all widths. Empirically, even the best channels detect only a small fraction of anomalies (well below the coverage threshold). This suggests that for independent channels, strict dimensionality reduction  $H < N$  can make per-channel monitoring infeasible without additional shared structure (e.g., correlations or low-rank factors) that allows compression without losing channel-level anomaly information.

**Feature-direction anomalies yield strong two-tailed detection for the Sign-Aware model.** We then evaluate feature-direction anomalies aligned to operational axes derived from a reference Sign-Aware model. We select  $M = 128$  directions by the standard deviation of the reference model’s gate preactivation on validation normals (top-std( $\pi$ )), and scale per-direction input perturbations using a fixed- $\Delta\pi$  rule to reduce width-dependent effects. We calibrate thresholds at 1% FPR and use localized pooling (max or top- $k$ ).

Across all widths, the Sign-Aware model achieves near-saturated directional recall and full direction coverage with max pooling (table 3). Non-sign-aware baselines remain near chance on this evaluation (directional recall close to the calibrated FPR and 0 coverage), consistent with their one-sided evidence and the difficulty of representing both tails of a direction efficiently under a fixed latent budget.

**Unbiased direction sets are not detectable under isotropic normals.** We repeat the feature-direction evaluation using:

- a fixed random orthonormal basis;
- PCA directions of the normal data.

Under isotropic normals these direction sets have no privileged alignment to a learned basis; all models (including Sign-Aware) achieve recall close to the calibrated FPR ( $\approx 1$ -2%) and 0 coverage across widths, even when we give non-sign-aware baselines  $2\times$  dictionary width. fig. 5 (right) visualizes this non-identifiability at  $H = 512$ .

An earlier feature-direction variant without strength control and using global sum pooling degrades sharply at larger widths: at  $H = 512$ , the Sign-Aware model drops to roughly 0.67 directional recall with near-zero coverage (16 seeds), motivating the fixed- $\Delta\pi$  scaling and localized pooling used above. fig. 5 visualizes this effect at  $H = 512$  by plotting the empirical CDF of per-direction two-tailed recall.

### D.3 Protocol C: Geometric Validation on Toy Models

**Setup.** We evaluate Protocol C described in §C.3, replicating the setup of [5] to provide visual and geometric confirmation that the Sign-Aware SAE correctly identifies and consolidates anticorrelated subspaces.

**Data Geometry.** We generate  $k$  pairs of features embedded in  $\mathbb{R}^2$  (the "unit circle" visualization), with paired directions that are antipodal on the unit circle. For the qualitative visualizations below, we use the mutually exclusive setting ( $\rho = -1$ ) so that exactly one member of each pair can be active at a time. We train models with dictionary width  $M = k$  (Sign-Aware) and  $M = 2k$  (Baseline),

Protocol B at H=512: distribution of two-tailed recall

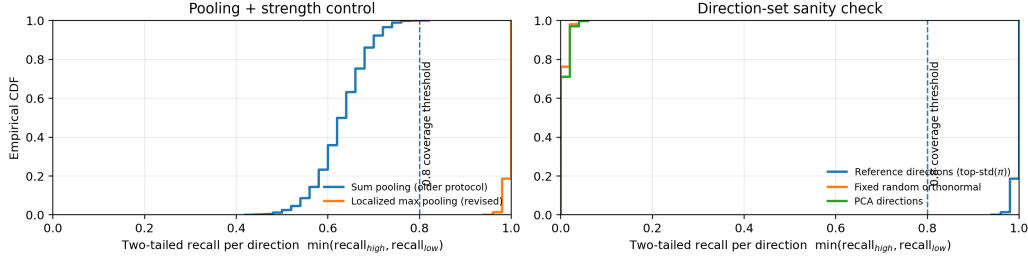


Figure 5: Protocol B (feature-direction anomalies) at  $H = 512$ : empirical CDF of per-direction two-tailed recall,  $\min(\text{recall}_{\text{high}}, \text{recall}_{\text{low}})$ , across directions and seeds. Left: the revised protocol with fixed- $\Delta\pi$  scaling, z-score normalization and localized max pooling concentrates above the 0.8 coverage threshold, while the earlier sum pooling variant degrades substantially. Right: direction-set sanity check under isotropic normals: when anomaly directions are fixed random orthonormal or PCA directions (independent of the reference), recall collapses to near-chance and coverage goes to zero, reflecting rotational non-identifiability.

so that in the ideal case the baseline allocates one latent per feature, while the Sign-Aware model allocates one latent per pair. Unless stated otherwise, we use  $k = 8$  for the qualitative visualizations and within-pair robustness sweep, and  $k = 16$  for the superposition sweep.

**Why Sign-Aware Consolidates Antipodal Pairs.** In the antipodal construction, each ground-truth pair corresponds to a single axis direction  $u_j \in \mathbb{R}^2$ , with two features at directions  $\pm u_j$ . In the mutually exclusive setting ( $\rho = -1$ ), an ideal Sign-Aware SAE can represent the entire pair using a single decoder column aligned with  $u_j$ : positive activations correspond to the  $+u_j$  feature and negative activations correspond to the  $-u_j$  feature. A non-negative SAE cannot use the sign of activations to flip direction, so representing both  $\pm u_j$  requires allocating two separate decoder columns, one per feature direction.

**Visualization A: The Unit Circle.** We project the columns of the decoder  $D$  onto the 2D data plane and plot them on the unit circle.

- **Baseline Observation:** Two distinct vectors at  $180^\circ$  separation (antipodal) for each feature pair. Each orange point should be matched to the nearest blue point on the same axis; nearby rather than exact overlap reflects ordinary optimization error.
- **Sign-Aware Observation:** A single vector per pair. The "negative" feature is represented by the negative activation of the same latent, rather than by an additional decoder vector.

**Visualization B: The Bi-Jump Histogram.** We collect activations for a single trained latent over the dataset and plot the histogram of  $a_i(x)$ .

The histogram reveals a tri-modal distribution: a large mass exactly at zero (the dead zone  $[-\delta_i^-, \delta_i^+]$ ), a lobe of positive activations, and a lobe of negative activations. This visually confirms the functionality of the Bi-Jump-ReLU activation function defined in eq. (5).

**Quantitative Sweep: Superposition Tolerance.** To obtain a transition-like quantitative curve, we fix the mutually exclusive antipodal construction ( $\rho = -1$ ) and vary the amount of superposition by changing the number of active pairs per sample (denoted  $n_{\text{active}}$ ). As  $n_{\text{active}}$  increases, multiple pairs contribute to each observation, and the model must represent signed pair membership in the presence of superposed features.

**Quantitative Metric: Signed Recoverability.** Let  $c_j(x)$  denote the signed ground-truth coefficient for pair  $j$ :  $c_j(x) > 0$  when the  $+u_j$  feature is active,  $c_j(x) < 0$  when the  $-u_j$  feature is active, and  $c_j(x) = 0$  otherwise. For each pair axis  $u_j$ , we consider latents whose decoder columns satisfy  $|\cos(D_{:,i}, u_j)| \geq \tau$  and orient their activations as  $\tilde{a}_i(x) = \text{sign}(D_{:,i}^\top u_j) a_i(x)$ , where  $D_{:,i}^\top u_j$  is the

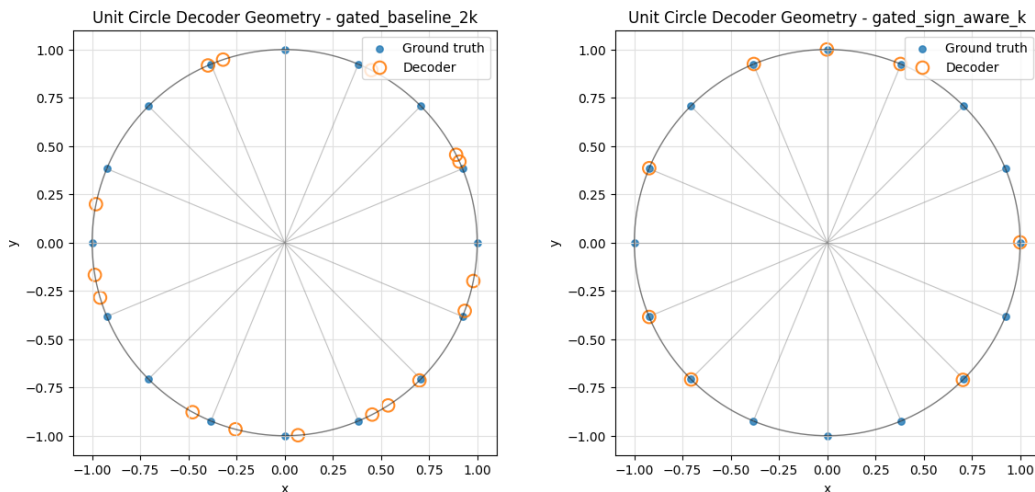


Figure 6: Protocol C qualitative geometry. Blue points mark the ground-truth feature directions on the unit circle, and orange points mark learned decoder columns projected into the same plane. In the mutually exclusive antipodal setting ( $\rho = -1$ ), a non-negative baseline at width  $M = 2k$  learns one decoder direction per feature, while the Sign-Aware SAE at width  $M = k$  learns one decoder direction per pair axis and uses activation sign to distinguish the two antipodal features. Exact overlap is not expected because training only recovers the generating axes approximately.

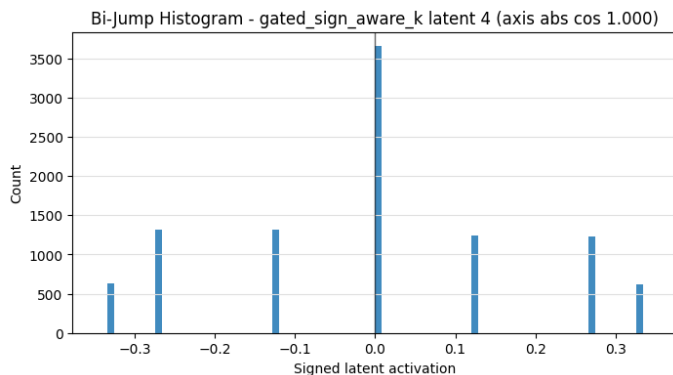


Figure 7: Bi-jump histogram for a representative Sign-Aware latent in Protocol C. The distribution exhibits two symmetric modes, consistent with a single latent representing an antipodal pair via positive vs negative activations.

dot product between the decoder column and the pair axis. Among these aligned latents, we select a single best candidate per pair using the same sign-consistency checks as in the consolidation metric below, and compute the Pearson correlation between  $\tilde{a}_{i^*(j)}(x)$  and  $c_j(x)$  over test samples where the pair is active. We report the mean of this best-candidate correlation across pairs as a continuous measure of signed recoverability.

**Thresholded Metric: Pair Consolidation Rate.** We also report the *Pair Consolidation Rate*, a stricter, thresholded variant of the above metric: the fraction of ground-truth pairs represented by a single latent that is both axis-aligned and sign-consistent.

We define that a ground-truth pair  $(j_1, j_2)$  is consolidated by latent  $i$  if:

- The decoder column  $D_{:,i}$  has absolute cosine similarity above a threshold  $\tau$  (e.g.,  $\tau = 0.9$ ) with the pair axis (equivalently, with both antipodal directions), and

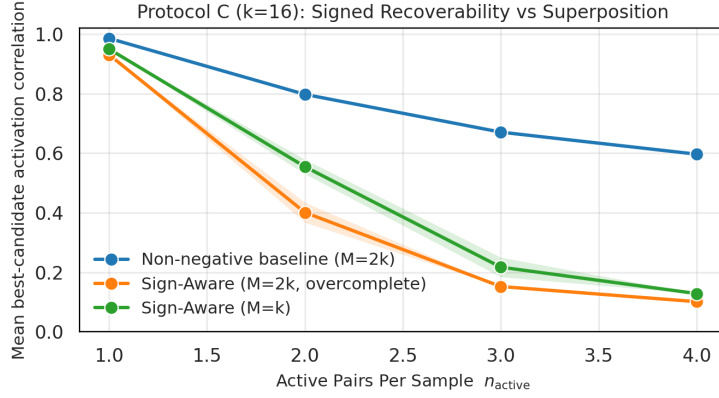


Figure 8: Protocol C quantitative curve (superposition tolerance,  $k = 16$ ): signed recoverability decreases as the number of active pairs per sample increases. We plot mean best-candidate activation correlation (mean  $\pm$  standard error (SE) over 16 seeds).

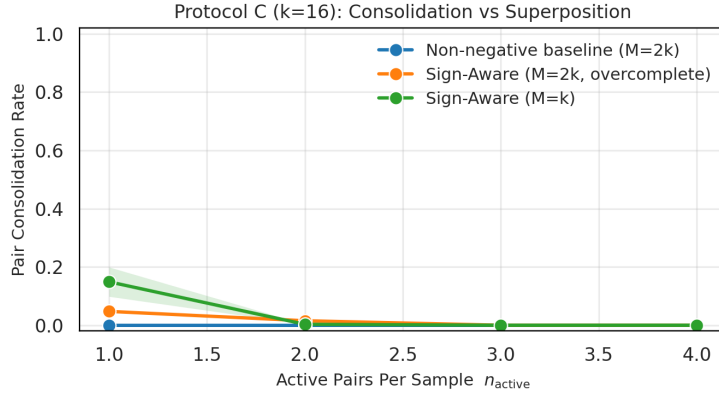


Figure 9: Thresholded Pair Consolidation Rate vs superposition in Protocol C (mean  $\pm$  SE over 16 seeds).

- The oriented activation  $\tilde{a}_i(x)$  is positively correlated with the signed ground-truth coefficient for the pair, and
- The sign of  $\tilde{a}_i(x)$  agrees with the ground-truth sign in both regimes (when  $+u_j$  is active vs when  $-u_j$  is active).

The Pair Consolidation Rate is the fraction of ground-truth pairs for which there exists at least one latent satisfying these conditions.

Signed recoverability shows a clear transition-like degradation with superposition (Fig. 8). The overcomplete Sign-Aware setting ( $M = 2k$ ) degrades faster, consistent with symmetry between one-latent and two-latent solutions.

The thresholded Pair Consolidation Rate collapses rapidly as superposition increases (Fig. 9), indicating that sign-consistent single-latent representations become unreliable under strong interference.

**Robustness Sweep: Within-Pair Correlation.** As a robustness check, we also sweep the within-pair correlation  $\rho$  from  $-1$  (mutually exclusive) to  $0$  (independent) at fixed  $n_{\text{active}} = 1$  and measure the Pair Consolidation Rate. This sweep produces a gradual degradation rather than a sharp transition, and is best interpreted as a robustness check rather than a phase transition.

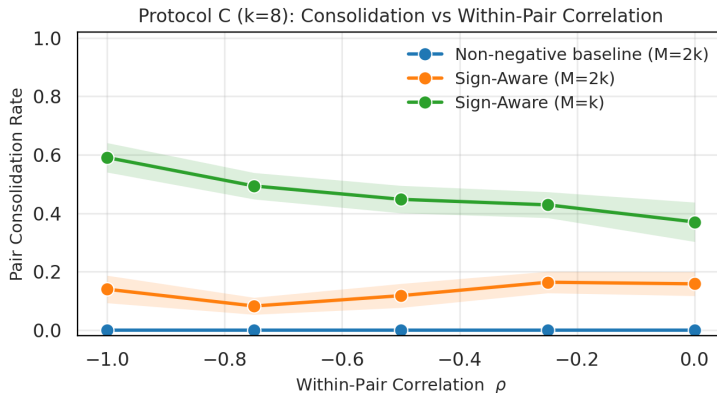


Figure 10: Robustness sweep: Pair Consolidation Rate vs within-pair correlation  $\rho$  at  $n_{\text{active}} = 1$  (mean  $\pm$  SE over 16 seeds).

## E LLM Ablations

**The auxiliary loss is essential.** Removing the auxiliary loss ( $\lambda_{\text{aux}} = 0$ ) is catastrophic: on Pythia-1B `m1p_out`, the entire  $\lambda$  sweep of the no-aux variant clamps at  $L_0 \in [1.7, 2.2]$  – the model fires effectively two latents per token regardless of  $\lambda$  – dead-fraction rises to 98%, and LR drops to 0.27. Without auxiliary supervision, gate parameters receive gradients only through the main reconstruction and sparsity terms, which is insufficient to learn effective two-sided detection. This confirms that the auxiliary frozen-decoder path is not merely a training convenience but a structural requirement for sign-aware gating.

**Symmetric magnitude is a viable simplification.** Tying the per-polarity magnitude scales ( $r_i^+ = r_i^-$ ) yields  $R^2 = 0.742 \pm 0.000$  and dead-fraction  $0.9\% \pm 0.0\%$  at matched  $L_0 = 64$ , versus  $R^2 = 0.741$  and dead-fraction  $0.8\%$  for the full SA-GSAE model – effect sizes of  $|\Delta R^2| = 0.0015$  and  $|\Delta \text{MSE}| = 0.0002$ , both practically negligible; the LR delta is within one standard error, and the dead-fraction delta ( $\approx 0.06$  pp) is  $\approx 2$  paired SE from zero but absolutely negligible. This weakens the Protocol-A suggestion that independent per-polarity scaling contributes on real LLM activations: on Pythia-1B `m1p_out`, it does not. The load-bearing elements of SA-GSAE at this operating point are the two-sided gating mechanism and the auxiliary reconstruction path; independent per-polarity magnitude asymmetry is a small second-order refinement at best.

**Dead-zone initialization exhibits a U-shape.** We sweep the initial dead-zone half-width  $\delta_0 \in \{10^{-3}, 10^{-2}, 0.5, 1.0\}$ , keeping all other hyperparameters fixed. Small initializations degrade reconstruction and inflate dead fraction:  $\delta_0 = 10^{-3}$  attains  $R^2 = 0.715$  and dead-fraction 27% at matched  $L_0 = 64$ , versus the reference  $R^2 = 0.741$  and 0.8% dead. Large initializations are neutral to mildly harmful:  $\delta_0 = 1.0$  attains  $R^2 = 0.744$  (marginally higher than the reference) with a slightly elevated dead-fraction of 7.8%. We recommend  $\delta_0 \in [0.1, 1.0]$  as a default; the common practice of initializing thresholds near zero actively harms capacity utilization.

**A reset-offsets variant is indistinguishable.** Enabling offset resets on dead-latent resampling (`reset_offsets_true`) yields  $R^2 = 0.741 \pm 0.000$  and dead-fraction  $0.8\% \pm 0.0\%$  at matched  $L_0 = 64$ , indistinguishable from the reference. We retain the default (no reset) for simplicity.

**Hybrid AbsTopK + gated magnitude is dominated by SA-GSAE.** To disentangle the contribution of sign-aware gating from the gated magnitude path, we evaluate a hybrid baseline that uses AbsTopK-style absolute selection (deterministic top- $k$  on  $|t_i(x)|$ ) but retains the gated magnitude computation from SA-GSAE. At matched  $L_0 = 64$ , this hybrid attains  $R^2 = 0.724 \pm 0.000$  and dead-fraction  $41\% \pm 0.4\%$ , both strictly worse than full SA-GSAE ( $R^2 = 0.741$ , dead-fraction 0.8%) and than AbsTopK alone on dead-fraction (0.0%). Fixed- $k$  absolute selection therefore does not combine favourably with the gated magnitude path – it neither matches AbsTopK’s dead-fraction floor nor

Table 4: Ablation study on Pythia-1B mlp\_out at matched  $L_0 = 64$  (mean  $\pm$  SE over 3 seeds). All variants use width  $H = 32,768$ .  $\delta_0$  denotes the initial dead-zone half-width. “no aux” did not reach  $L_0 = 64$ : its sweep clamps at  $L_0 \in [1.7, 2.2]$ ; we report its metrics at the maximum attained  $L_0$  rather than at  $L_0 = 64$  and flag the row accordingly.

Variant	LR $\uparrow$	$R^2$ $\uparrow$	MSE $\downarrow$	Dead $\downarrow$
SA-GSAE, full (reference)	0.785 (0.002)	0.741 (0.000)	0.0375 (0.0000)	0.008 (0.001)
SA-GSAE, sym. mag. ( $r^+ = r^-$ )	0.784 (0.002)	<b>0.742</b> (0.000)	<b>0.0373</b> (0.0000)	0.009 (0.000)
SA-GSAE, reset offsets	0.781 (0.000)	0.741 (0.000)	0.0375 (0.0000)	0.008 (0.000)
SA-GSAE, $\delta_0 = 1.0$	0.788 (0.001)	0.744 (0.000)	<b>0.0371</b> (0.0000)	0.078 (0.000)
SA-GSAE, $\delta_0 = 0.5$	<b>0.789</b> (0.002)	0.743 (0.000)	<b>0.0371</b> (0.0000)	0.044 (0.001)
SA-GSAE, $\delta_0 = 10^{-2}$	0.777 (0.003)	0.733 (0.001)	0.0387 (0.0001)	0.018 (0.002)
SA-GSAE, $\delta_0 = 10^{-3}$	0.757 (0.003)	0.715 (0.001)	0.0413 (0.0001)	0.269 (0.003)
Hybrid AbsTopK + gated mag	0.773 (0.001)	0.724 (0.000)	0.0400 (0.0000)	0.414 (0.004)
SA-GSAE, no aux <sup>†</sup>	0.278 <sup>†</sup>	0.353 <sup>†</sup>	0.094 <sup>†</sup>	0.978 <sup>†</sup>
Gated SAE, full (baseline)	0.761 (0.003)	0.711 (0.001)	0.0419 (0.0001)	0.737 (0.004)
AbsTopK, full (baseline)	0.746 (0.002)	0.666 (0.000)	0.0484 (0.0000)	<b>0.000</b> (0.000)

<sup>†</sup> reported at the max attained  $L_0 \approx 2$ , not at  $L_0 = 64$ ; the sweep never reaches  $L_0 = 64$ .

matches SA-GSAE’s reconstruction quality – which clarifies that learned two-sided thresholds with auxiliary supervision drive both capacity utilization and reconstruction quality jointly, rather than being separable into a selection and a magnitude component.

## F Full-Width SA-GSAE Results

For completeness, at matched  $L_0 \approx 64$  on all six hookpoint  $\times$  backbone cells, full-width SA-GSAE ( $H = 32,768$ ) is well-behaved on five of six cells: it attains the best  $R^2$  on mlp\_out-mid/Pythia-1B, mlp\_out-mid/SmolLM3-3B, and resid-mid/Pythia-1B, and is within 0.016 of the best  $R^2$  on the remaining two non-collapsing cells.

The sixth cell, resid-mid/SmolLM3-3B, exhibits a *reproducible reconstruction collapse*: at the matched operating point of  $L_0 = 64$ , full-width SA-GSAE attains  $\text{MSE} = 1.15 \pm 0.22$  and  $R^2 = -0.006 \pm 0.189$ , whereas every other variant on the same cell remains at  $\text{MSE} \leq 0.01$  and  $R^2 \geq 0.99$ . table 5 shows the per-seed  $\lambda$  sweep for this cell. All three seeds start well-behaved at  $\lambda \leq 2.4 \cdot 10^{-4}$  ( $L_0 \approx 270$  to  $760$ ,  $\text{MSE} \approx 0.003$ ,  $R^2 \geq 0.995$ ), then enter a regime where reconstruction fidelity degrades sharply: MSE inflates to 0.2–6.0 at interior  $\lambda$  values,  $R^2$  drops to as low as  $-4.3$ , and 3 of 24 sweep points fall below  $\text{LR} = 0.5$ , one on each of seeds 0, 1, and 2, at  $\lambda \in \{2.44 \cdot 10^{-3}, 3.89 \cdot 10^{-3}\}$  (the two largest sparsity coefficients). The worst-case sweep point is seed 2 at  $\lambda = 3.9 \cdot 10^{-3}$ :  $\text{loss}_{\text{reconstructed}} = 10.25$  is only 1.51 nats below  $\text{loss}_{\text{ablated}} = 11.76$ , so the reconstruction recovers only  $\text{LR} = 0.175$  of the ablation gap. The reconstruction never strictly worsens relative to ablation, but it comes within  $\sim 1.5$  nats of doing so.

The half-width SA-GSAE on the same cell is monotone on 3/3 seeds,  $R^2 \geq 0.985$  at every sparsity point, and MSE never exceeds 0.018. This contrast – catastrophic at full width, clean at half width, on the same data and training protocol – motivates the halved-width operating point not only theoretically (sign-aware latents carry double the information, so  $H_{\pm} = H$  suffices) but also as a practical hedge against catastrophic optimization regimes at specific activation sites. We do not yet have a mechanistic explanation for why only this particular cell collapses; candidate hypotheses include the very large dynamic range of the residual stream interacting with the two-sided gate threshold warmup, or over-parameterization combined with sign-aware auxiliary supervision driving the optimizer into a degenerate minimum. A targeted warmup-schedule ablation would disambiguate these and is a natural follow-up.

## G Full-Distribution Calibration and Bipolar Census

This appendix supplements the §Results block on calibration symmetry and bipolar-latent usage (tables 6 and 8) with per-cell CDFs of  $\gamma_{\pm}$  and an extended bipolar census over two polarity-imbalance thresholds.

Table 5: Per-seed  $\lambda$  sweep of full-width SA-GSAE on resid-mid/SmolLM3-3B. MSE values inside the collapse regime ( $\text{MSE} > 0.1$ ) are bolded; the bolded cells are the same rows in which  $R^2$  drops below 0.85 and the LM-loss gap closes substantially. The baseline losses are  $\text{loss\_original} = 3.153$  and  $\text{loss\_ablated} = 11.762$  (identical across variants);  $\text{loss\_reconstructed}$  never strictly exceeds  $\text{loss\_ablated}$  but comes within 1.51 nats of it at the worst-case sweep point (seed 2,  $\lambda = 3.9 \cdot 10^{-3}$ ).

Seed	$\lambda$	$L_0$	MSE	$R^2$	loss_reconstructed
0	$1.48 \cdot 10^{-4}$	761.06	0.0032	0.997	3.143
	$2.36 \cdot 10^{-4}$	273.87	0.0052	0.995	3.188
	$3.77 \cdot 10^{-4}$	113.02	<b>0.234</b>	0.795	3.585
	$6.01 \cdot 10^{-4}$	72.31	<b>1.738</b>	-0.520	4.376
	$9.59 \cdot 10^{-4}$	48.32	0.072	0.937	3.716
	$1.53 \cdot 10^{-3}$	35.77	<b>2.509</b>	-1.20	6.634
	$2.44 \cdot 10^{-3}$	26.64	<b>1.641</b>	-0.436	5.894
1	$3.89 \cdot 10^{-3}$	31.56	<b>0.733</b>	0.359	7.637
	$1.48 \cdot 10^{-4}$	751.39	0.0032	0.997	3.170
	$2.36 \cdot 10^{-4}$	271.91	0.0057	0.995	3.162
	$3.77 \cdot 10^{-4}$	108.86	<b>1.236</b>	-0.081	4.034
	$6.01 \cdot 10^{-4}$	75.10	<b>0.191</b>	0.833	3.875
	$9.59 \cdot 10^{-4}$	48.92	<b>1.669</b>	-0.460	4.730
	$1.53 \cdot 10^{-3}$	40.51	<b>0.625</b>	0.454	4.659
2	$2.44 \cdot 10^{-3}$	28.37	<b>6.015</b>	-4.26	8.182
	$3.89 \cdot 10^{-3}$	27.24	<b>0.212</b>	0.814	6.964
	$1.48 \cdot 10^{-4}$	755.40	0.0032	0.997	3.129
	$2.36 \cdot 10^{-4}$	276.24	0.0052	0.995	3.186
	$3.77 \cdot 10^{-4}$	112.51	<b>0.183</b>	0.840	3.660
	$6.01 \cdot 10^{-4}$	67.95	<b>1.359</b>	-0.189	5.566
	$9.59 \cdot 10^{-4}$	49.66	<b>1.967</b>	-0.721	6.527
	$1.53 \cdot 10^{-3}$	33.43	<b>0.220</b>	0.807	4.252
	$2.44 \cdot 10^{-3}$	26.95	<b>0.632</b>	0.447	6.692
	$3.89 \cdot 10^{-3}$	29.81	<b>3.660</b>	-2.20	10.251

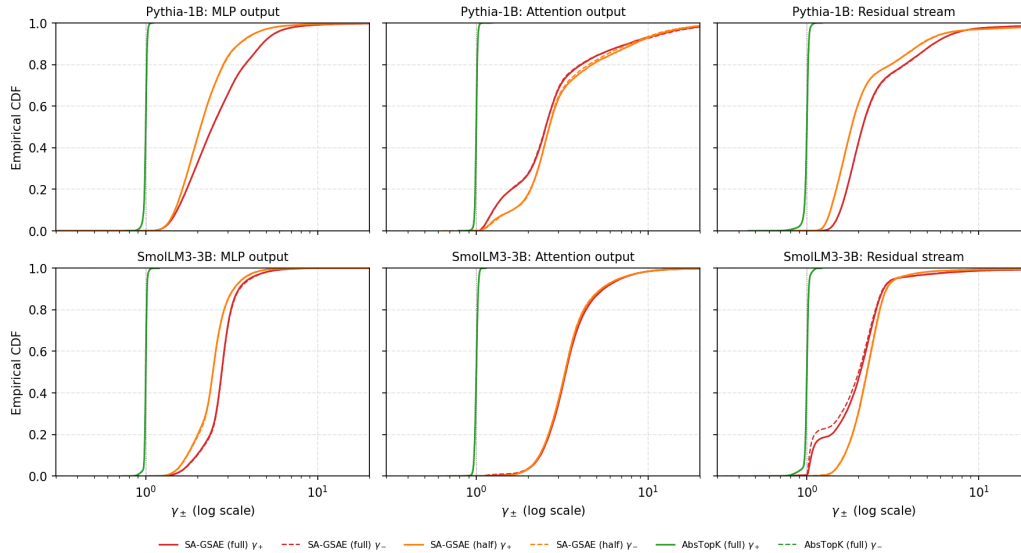


Figure 11: Empirical CDFs of per-latent calibration slopes  $\gamma_+$  (solid) and  $\gamma_-$  (dashed), pooled across all valid latents and 3 seeds at matched  $L_0 \approx 64$ . Top row: Pythia-1B at MLP output / attention output / residual stream. Bottom row: SmolLM3-3B at the same three hookpoints. Curves are shown for SA-GSAE (full), SA-GSAE (half), and AbsTopK (full). The dotted vertical line at  $\gamma = 1$  marks the ideal. Two structural observations hold on every cell: (i) solid and dashed curves for each variant are essentially superimposed, i.e. the  $\gamma_+$  and  $\gamma_-$  distributions are symmetric; (ii) SA-GSAE’s distribution is concentrated near  $\gamma \in [1.5, 5]$  while AbsTopK’s collapses onto  $\gamma \approx 1$ , which follows mechanically from AbsTopK’s lack of a learnable dead zone and is not a calibration-training advantage (section B).

Table 6: Full bipolar-latent census at matched  $L_0 = 64$  (mean  $\pm$  SE over 3 seeds) over both polarity-imbalance thresholds. “Bipolar  $< \theta$ ” is the fraction of alive latents with  $I_i < \theta$ . Ranking between SA-GSAE and AbsTopK is stable across  $\theta \in \{0.3, 0.5\}$ .

Cell	Variant	$L_0$	Alive frac	Bipolar $< 0.3$	Bipolar $< 0.5$	$\hat{p}$
Pythia-1B / mlp_out	SA-GSAE (full)	64.6	0.992 (0.001)	0.053 (0.001)	0.097 (0.001)	0.300 (0.001)
	SA-GSAE (half)	66.4	0.998 (0.000)	0.062 (0.001)	0.090 (0.001)	0.283 (0.002)
	AbsTopK (full)	64.0	1.000 (0.000)	0.940 (0.001)	0.994 (0.000)	1.000 (0.000)
	AbsTopK (half)	64.0	1.000 (0.000)	0.945 (0.001)	0.992 (0.000)	1.000 (0.000)
SmolLM3-3B / mlp_out	SA-GSAE (full)	66.0	0.994 (0.000)	0.287 (0.003)	0.429 (0.003)	0.707 (0.005)
	SA-GSAE (half)	65.9	0.999 (0.000)	0.279 (0.005)	0.387 (0.004)	0.767 (0.004)
	AbsTopK (full)	64.0	1.000 (0.000)	0.932 (0.002)	0.997 (0.000)	1.000 (0.000)
	AbsTopK (half)	64.0	1.000 (0.000)	0.960 (0.000)	0.996 (0.000)	1.000 (0.000)
Pythia-1B / attn	SA-GSAE (full)	64.6	0.226 (0.003)	0.065 (0.005)	0.100 (0.008)	0.077 (0.003)
	SA-GSAE (half)	64.6	0.429 (0.002)	0.051 (0.003)	0.080 (0.003)	0.141 (0.001)
	AbsTopK (full)	64.0	0.498 (0.001)	0.649 (0.002)	0.862 (0.002)	0.603 (0.003)
	AbsTopK (half)	64.0	0.843 (0.005)	0.709 (0.003)	0.911 (0.002)	0.902 (0.006)
SmolLM3-3B / attn	SA-GSAE (full)	65.4	0.370 (0.019)	0.115 (0.007)	0.188 (0.011)	0.162 (0.000)
	SA-GSAE (half)	65.4	0.679 (0.021)	0.124 (0.003)	0.203 (0.004)	0.322 (0.005)
	AbsTopK (full)	64.0	0.968 (0.001)	0.639 (0.002)	0.884 (0.001)	0.981 (0.001)
	AbsTopK (half)	64.0	1.000 (0.000)	0.724 (0.002)	0.938 (0.001)	1.000 (0.000)
Pythia-1B / resid	SA-GSAE (full)	65.4	0.995 (0.000)	0.089 (0.002)	0.162 (0.002)	0.439 (0.003)
	SA-GSAE (half)	68.0	1.000 (0.000)	0.099 (0.003)	0.175 (0.004)	0.481 (0.005)
	AbsTopK (full)	64.0	1.000 (0.000)	0.865 (0.003)	0.981 (0.001)	1.000 (0.000)
	AbsTopK (half)	64.0	1.000 (0.000)	0.878 (0.003)	0.973 (0.001)	1.000 (0.000)
SmolLM3-3B / resid	SA-GSAE (full)	64.9	0.596 (0.007)	0.007 (0.001)	0.013 (0.001)	0.039 (0.001)
	SA-GSAE (half)	64.1	0.845 (0.016)	0.043 (0.005)	0.052 (0.004)	0.082 (0.003)
	AbsTopK (full)	64.0	1.000 (0.000)	0.859 (0.001)	0.985 (0.000)	1.000 (0.000)
	AbsTopK (half)	64.0	1.000 (0.000)	0.876 (0.001)	0.980 (0.000)	1.000 (0.000)

### G.1 Sweep-based Pareto dominance summary (SA-half vs. Gated-full)

This subsection replaces the retired matched- $L_0 = 64$  tables as the reproducibility anchor for the Pareto comparison between half-width SA-GSAE ( $H = 16,384$ ) and full-width Gated SAE ( $2H = 32,768$ ). For each of the six hookpoint  $\times$  backbone cells we compute, on a 2000-point geometric grid in  $\log L_0$  over the overlap of the two variants’ swept  $L_0$  means, (i) the fraction of the grid on which SA-half strictly Pareto-dominates Gated-full (SA-half  $R^2 \geq$  Gated-full  $R^2$  and SA-half dead-fraction  $\leq$  Gated-full dead-fraction), (ii) the median and geometric-mean dead-fraction reduction ratio (Gated-full / SA-half), (iii) the peak ratio and the  $L_0$  at which it occurs, and (iv) the signed extremum of  $\Delta R^2 = R^2_{\text{SA-half}} - R^2_{\text{Gated-full}}$ . All statistics are linear-interpolated in  $\log L_0$  between adjacent  $\lambda$ -sweep aggregate points.

Table 7: Sweep-based Pareto summary. “Dom. frac.” is the fraction of the overlap  $L_0$  grid on which SA-half strictly Pareto-dominates Gated-full (strict  $\epsilon = 0$ ). Peak ratio ( $L_0^{\text{peak}}$ ) is the argmax of Gated-full dead / SA-half dead on the overlap grid. On attention cells and resid-mid/SmolLM3-3B (marked  $\dagger$ ), SA-half also dominates a larger region under a noise-tolerant variant  $\epsilon_{R^2} = 10^{-3}$  (at or below the per-sweep-point  $R^2$  SE): the tolerant dominance regions are  $L_0 \in [13.7, 25.3]$  (31%) on Py/attn,  $L_0 \in [4.8, 43.3]$  (69%) on SmolLM3/attn, and  $L_0 \in [36.9, 111.9]$  (54%) on SmolLM3/resid. Signed  $\Delta R^2$  extrema are reported in the main-body Pareto paragraph.

Backbone	Hookpoint	Overlap $L_0$	Dom. frac.	Median / Geomean / Peak ratio ( $L_0^{\text{peak}}$ )
Pythia-1B	mlp_out	[15.3, 144.4]	100%	155 $\times$ / 145 $\times$ / 671 $\times$ (98.5)
	attn	[13.7, 97.8]	26% $\dagger$	1.5 $\times$ / 1.5 $\times$ / 1.6 $\times$ (67.7)
	resid	[17.9, 129.3]	100%	191 $\times$ / 492 $\times$ / 1.49 $\cdot 10^4$ (129.3)
SmolLM3-3B	mlp_out	[5.4, 127.4]	100%	60 $\times$ / 96 $\times$ / 1.03 $\cdot 10^4$ (127.4)
	attn	[4.8, 116.0]	66% $\dagger$	2.2 $\times$ / 2.1 $\times$ / 3.1 $\times$ (50.3)
	resid	[21.1, 111.9]	10% $\dagger$	2.0 $\times$ / 4.0 $\times$ / 709 $\times$ (111.9)

### G.2 Per-cell $\gamma_{\pm}$ distribution summary

Table 8:  $\gamma_+$  and  $\gamma_-$  distribution summaries at matched  $L_0 = 64$  (mean over 3 seeds). Medians agree within  $\leq 0.05$  and  $[p_{10}, p_{90}]$  intervals overlap almost exactly on every cell, supporting the symmetric-magnitude default  $r_i^+ = r_i^-$ . AbsTopK’s tight spike at  $\gamma \approx 1$  is a mechanical consequence of its architecture (no dead zone; see App. B), not a calibration-training win.

Cell	Variant	$\gamma_+$			$\gamma_-$		
		median	$p_{10}$	$p_{90}$	median	$p_{10}$	$p_{90}$
Pythia-1B / mlp_out	SA-GSAE (full)	2.42	1.52	4.68	2.41	1.52	4.67
	SA-GSAE (half)	2.20	1.52	3.78	2.21	1.52	3.80
	AbsTopK (full)	1.00	0.97	1.02	1.00	0.97	1.02
SmoLLM3-3B / mlp_out	SA-GSAE (full)	2.63	1.89	3.26	2.64	1.90	3.29
	SA-GSAE (half)	2.38	1.68	3.10	2.38	1.69	3.13
	AbsTopK (full)	1.00	0.98	1.02	1.00	0.98	1.02
Pythia-1B / attn	SA-GSAE (full)	2.53	1.26	7.63	2.52	1.27	7.66
	SA-GSAE (half)	2.64	1.62	8.17	2.64	1.61	7.85
	AbsTopK (full)	1.00	0.98	1.02	1.00	0.98	1.02
SmoLLM3-3B / attn	SA-GSAE (full)	3.23	2.31	5.32	3.23	2.30	5.30
	SA-GSAE (half)	3.21	2.28	5.15	3.19	2.28	5.14
	AbsTopK (full)	1.00	0.97	1.03	1.00	0.97	1.03
Pythia-1B / resid	SA-GSAE (full)	2.05	1.53	5.34	2.05	1.53	5.36
	SA-GSAE (half)	1.90	1.41	4.68	1.90	1.41	4.64
	AbsTopK (full)	1.00	0.96	1.03	1.00	0.96	1.03
SmoLLM3-3B / resid	SA-GSAE (full)	2.02	1.06	2.73	1.98	1.04	2.70
	SA-GSAE (half)	2.22	1.65	2.87	2.20	1.64	2.86
	AbsTopK (full)	1.00	0.97	1.03	1.00	0.97	1.03

### G.3 Qualitative latent semantics

**Qualitative latent semantics.** We inspect the top-64 latents by absolute activation magnitude from SA-GSAE full-width checkpoints, one per hookpoint  $\times$  backbone (seed 0; 6 files in total from the examples stage). Classifying each latent as *bipolar* when its weaker-sign peak is within a factor of three of its stronger-sign peak, *positive-only* or *negative-only* when one sign peak is at least ten times the other, and *sign-dominant* otherwise, we find that bipolar structure concentrates at attention hookpoints: 12/64 (19%) of top-64 latents on attn-mid/Pythia-1B, 3/64 (5%) on attn-mid/SmoLLM3-3B, and 5/64 (8%) on resid-mid/Pythia-1B; MLP-output hookpoints and resid-mid/SmoLLM3-3B exhibit 0–1 bipolar latents per file under this criterion and are dominated by sign-monopolar features. This matches the paper’s theoretical picture (sign-aware latents are most useful where bidirectional semantic structure is actually present) and also sharpens it (bidirectional structure is hookpoint-specific). Representative latents are collected in table 9: for each backbone we show one bipolar, one positive-only and one negative-only latent, covering all three mid-depth hookpoints. The Pythia attn bipolar latent 22641 is the paper’s motivating case – its positive side fires inside the “Parent Revolution” education-astroturf sentence while its negative side fires on Murdoch-owned-media and product-pitch boilerplate, carrying anticorrelated real-world evidence along one decoder direction. The SmoLLM3 mlp\_out bipolar latent 26596 makes the same point at a structural level: its positive side fires on expository sentence endings while its negative side fires on mid-turn dialogue continuations, showing that sign-sharing also captures contrasts

that are syntactic rather than topical. The human-interpretable descriptions in table 9 (“education-reform astroturf”, “Murdoch-owned media”, etc.) were produced by the Amazon Kiro assistant from the top- $N$  positive and negative activation contexts of each selected latent.

Table 9: Selected qualitative latents from SA-GSAE full-width checkpoints, seed 0. For each backbone we show one bipolar, one positive-only and one negative-only latent, covering all three mid-depth hookpoints. Each positive/negative cell gives a human-interpretable description followed by one representative activation in italics, with the activating token rendered in **bold**; empty cells correspond to the inactive sign of a one-sided latent.

Model / hookpoint	Category	Latent	Positive	Negative
Pythia-1B / attn	bipolar	22641	Education-reform astroturf sentences (“Parent Revolution”, Excellence-in-Education Foundation, ALEC): <i>released this month. trickster group Parent <b>Revolution</b>, the spark for the current “W</i>	Murdoch-owned-media and corporate-pitch boilerplate: <i>Wireless Generation is owned by Rupert <b>Murdoch</b>, who also owns Fox News and the Wall Street Journal.</i>
Pythia-1B / mlp_out	positive-only	18628	Cross-article boundary: fires immediately after an <code>&lt; endoftext &gt;</code> token as a new article begins: <i>reach out to us @Algorithmia.&lt;endoftext&gt;As more activists call attention</i>	
Pythia-1B / attn	negative-only	14958		Progressive / social-justice critique of corporate education reform (MLK citations, anti-privatization discourse): <i>quotes Martin Luther King’s <b>Letter</b> from a Birmingham Jail . . . progressives with a strong belief in social justice</i>
SmolLM3-3B / mlp_out	bipolar	26596	End-of-clause punctuation in expository/narrative prose (completed sentence boundaries): <i>Global Energy Mining and Minerals <b>Limited</b>, a Hungarian company, and</i>	Mid-turn continuations in dialogue or interior monologue: <i>but Hugh refuses to reveal <b>what</b> he knows about the situation</i>
SmolLM3-3B / mlp_out	positive-only	20224	Transliteration-table entries for proper nouns across Asian languages (Mandarin / Japanese / Korean / Vietnamese): <i>Mandarin [Xiū] <b>Transliteration</b> of his Japanese name Russian</i>	
SmolLM3-3B / attn	negative-only	19176		Video-game dialogue turns (Pokémon-franchise NPC lines and interior-monologue asides embedded in web text): <i>“There might be more in there!” “Could you be Gym <b>Leader</b> Burgh?” “Is that . . . so?”</i>

## H Licenses

Licenses checked on 21.03.2026.

Table 10: Hosted LLM benchmark assets, licenses, and URLs.

Type	Asset	License
Model	EleutherAI/pythia-1b	Apache 2.0
	URL: <a href="https://huggingface.co/EleutherAI/pythia-1b">https://huggingface.co/EleutherAI/pythia-1b</a>	
Model	HuggingFaceTB/SmolLM3-3B	Apache 2.0
	URL: <a href="https://huggingface.co/HuggingFaceTB/SmolLM3-3B">https://huggingface.co/HuggingFaceTB/SmolLM3-3B</a>	
Dataset	OpenWebText	CC0
	URL: <a href="https://skylion007.github.io/OpenWebTextCorpus">https://skylion007.github.io/OpenWebTextCorpus</a>	